Equivalent material properties of the heat-affected zone in welded cold-formed rectangular hollow section connections

Yan, Rui; Mela, Kristo; Yang, Fei; El Bamby, Hagar; Veljkovic, Milan

DOI
10.1016/j.tws.2022.110479

Publication date
2023

Document Version
Final published version

Published in
Thin-Walled Structures

Thin-Walled Structures 184 (2023) 110479

Contents lists available at ScienceDirect

Thin-Walled Structures

journal homepage: www.elsevier.com/locate/tws

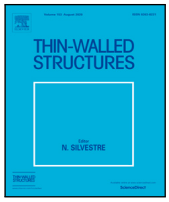

Full length article

Equivalent material properties of the heat-affected zone in welded cold-formed rectangular hollow section connections

Rui Yan [a,*], Kristo Mela [b], Fei Yang [c], Hagar El Bamby [a], Milan Veljkovic [a]

[a] Department of Engineering Structures, Delft University of Technology, Delft, The Netherlands
[b] Faculty of Built Environment, Tampere University, Tampere, Finland
[c] School of Civil Engineering, Chang'an University, Xi'an, China

ARTICLE INFO

Keywords:
Heat-affected zone
Transverse constraint
High-strength steel
Butt weld
Constitutive model

ABSTRACT

A welded connection consists of three main material zones, the base material (BM), the heat-affect zone (HAZ), and the weld metal (WM). The strength of HAZ depends on the BM grade and manufacturing process, electrode grade, and welding parameters. Under certain conditions, HAZ has the lowest material strength, especially for high-strength steel. Therefore, a semi-empirical methodology is proposed to establish a constitutive model of HAZ necessary for predicting the fracture position of welded connections. This methodology is based on an engineering approach to consider HAZ as an isotropic and homogeneous material, with no consideration of different volumetric fractions of microstructures within a HAZ. The equivalent material properties of HAZ in butt-welded hollow section connections were investigated experimentally and numerically. Hardness tests and microstructure investigations were conducted to determine the boundaries of material variations and the width of HAZ. The stress–strain relationship of HAZ was established and calibrated based on tensile coupon tests and finite element analyses. Using the calibrated HAZ stress–strain relationship, the effect of transverse constraint imposed by the adjacent and stronger material (BM and WM) on HAZ was evaluated in the welded connections. Finally, the new methodology of a semi-empirical constitutive model based on the Swift model was used to propose equivalent characteristics of HAZ as a function of the mechanical properties of BM for a specific welding procedure considered in the project.

1. Introduction

In steel construction, welding is one of the most essential methods of joining steel parts. A welded connection comprises three main zones, namely the base material (BM), the heat-affected zone (HAZ), and the weld metal (WM). The mechanical properties of HAZ depend on several parameters, such as the steel manufacturing process, the cooling time from 800 °C to 500 °C ($t_{8/5}$) during welding, and the heat input. HAZ may have comparable strength to BM for Quenching and Tempering (QT) steels with a low heat input [1–3]. Otherwise, a significant strength degradation in HAZ may be observed for QT and Thermo-Mechanically Controlled Process (TMCP) steels [4,5], especially for high-strength steels (HSS). The difference in the strength degradation in HAZ could also be observed from the hardness test results, as the hardness reflects the material strength. The test results available in literature, which have similar steel grades to the material investigated in this study, are presented in Table 1. A limited strength degradation in HAZ was observed from S420 and S500 materials with low heat input, while the strength degradation in S700 may reach up to 23%, as found in [6].

In the case of welded connections with a reduced material strength of HAZ compared to BM and WM, a transverse constraint on the deformation of HAZ is imposed during tensile loading [5,10]. Therefore, it is crucial to understand both phenomena, the strength reduction and the transverse constraint leading to strength increase in HAZ, to properly evaluate and predict the behaviour of welded connections.

The design rules for welded connections (up to S460) in EN 1993-1-8 [11] do not consider the strength reduction in HAZ and the strength enhancement due to the transverse constraint. Since the strength reduction in HAZ is rather limited for mild steels in practical applications, it is reasonable to design the connection without considering the effect of HAZ. The new version of prEN 1993-1-8 [12] stipulates that the strength of the filler metal should be included in design of a butt weld if BM is higher than S460 and different filler metal and BM are used. However, for HSS and ultra-high-strength steel (UHSS, steel grade higher than S700), the strength of HAZ may be significantly lower than BM and WM. Using only the strength of filler metal in the design may lead to an unsafe prediction of the connection resistance. On the other hand, the resistance of the HAZ could be significantly improved by the strong transverse constraint from BM and WM. Consequently, the

* Corresponding author.
E-mail address: r.yan@tudelft.nl (R. Yan).

https://doi.org/10.1016/j.tws.2022.110479
Received 26 July 2022; Received in revised form 28 November 2022; Accepted 15 December 2022
Available online xxxx

Table 1
Comparison of HAZ hardness reduction.

References	Steel grade	Yield strength [MPa]	Processing method	Heat input [kJ/mm]	Hardness reduction in HAZ [%]
Pisarski and Dolby, 2003 [7]	RQT 501	550	QT	2.40	16–24
Hochhauser et al. 2012 [8]	S700	700	TMCP	0.42–0.76	12–16
Khurshid et al. 2015 [9]	S700	700	TMCP	0.41	16
Nguyen, 2018, [6]	S420	420	TMCP	0.48–1.48	0.3–7.5
	S500	500		0.48–1.47	1.7–12
	S700	700		0.61–1.37	19–23
Cai et al. 2022, [4]	Q550	550	QT	1–1.9	9–15
	Q550	550	TMCP	1–1.9	11–17
	Q690	690	QT	1–1.9	9–20
	Q690	690	TMCP	1–1.9	15–21

effect of transverse constraints on both the strength degradation and the strength enhancement in HAZ should be considered to provide a safe and economical design recommendation for welded connections made of HSS and UHSS.

In this paper, nine butt-welded cold-formed rectangular hollow section connections, encompassing three steel grades and three thicknesses, were used to investigate the geometric and mechanical properties of HAZ. First, the low-force Vickers hardness tests and microstructure observation were conducted to determine the width of HAZ and investigate the hardness deterioration in HAZ. Then, the stress–strain relationship of HAZ was established and calibrated based on the tensile coupon tests and finite element analysis (FEA) using the equivalent material approach introduced in Section 2. A new methodology of a semi-empirical constitutive model following the Swift model [13] is proposed for HAZ, based on the mechanical properties of BM. Finally, using the calibrated HAZ stress–strain relationship, an attempt was made to reveal the effect of transverse constraint on the resistance of welded connections under the coupon specimen scale level and the hollow section scale level.

2. State of the art

The stress–strain relationship of HAZ plays a crucial role in the numerical analysis of welded connections [5]. Three approaches have been proposed in the literature to directly obtain the HAZ stress–strain relationship from the tensile coupon tests. In the first approach (micro specimen approach), a micro tensile coupon specimen fabricated from a single material zone, such as HAZ, can be used to establish the stress–strain constitutive model [14–17]. The advantage of this method is that the stress and strain of a single zone could be directly measured from the experiment, provided that the testing material in one specimen is homogeneous. However, the microstructure of HAZ varies in directions perpendicular to the welding seam direction, resulting in an irregular width of HAZ. It is rather difficult to ensure the homogeneity of the material in the micro-specimen. In addition, the fabrication and testing procedures are time-consuming and costly compared to the standard coupon tests. Alternatively, a thermal simulation machine can be employed to reproduce the temperature–time history in different HAZ sub-zones of a welded connection [2,18]. In this approach (thermal simulation approach), the thermal cycles are applied on steel plates to make the microstructure identical to the corresponding HAZ sub-zone. Note that obtaining a homogeneous HAZ microstructure is essential for this method in order to correctly calibrate the material model for each zone. Finally, the constitutive models of each HAZ sub-zones are obtained using the coupon specimens fabricated from the thermal-treated plates.

In another (semi-)direct approach (equivalent material approach), a coupon specimen with a butt weld in the middle transverse to the loading direction is tested in tension to establish the stress–strain relationship of HAZ and WM, using the digital image correlation (DIC) measuring technique [19–28]. The specimen is often milled to a thin layer before testing to obtain a constant width of HAZ through the thickness. Note that the measured stress–strain relationship of WM is extended using a theoretical model to complete the relationship when the weld failure does not occur. This approach is often accompanied by an inverse method to calibrate the material constitutive model of HAZ with the aid of finite element (FE) analysis. In the inverse method, the constitutive model is calibrated by fitting the FE results to the experimental results. The key parameters are adjusted based on the difference between FE and experimental results. The stress is obtained based on the uniform stress assumption [19], which is the total load divided by the cross-sectional area. The strain is derived using the measured local deformation of each zone. Note that the initial gauge length for measuring the local deformation may vary in different zones.

Two issues should be addressed to establish a proper constitutive model using the equivalent material approach. Firstly, although a high-strain region during the tensile test could be observed in DIC results, determining the measuring gauge length of HAZ is not straightforward as the boundary of HAZ is vague. In addition, the identified width of HAZ and WM are required for generating the FE model to calibrate the constitutive model using the inverse method. Yan et al. [10] proposed a method to identify the boundary of HAZ based on the different stress states in HAZ (biaxial in tension) and BM/WM (combined tension and compression) at the plastic deformation stage. The different stress states result from the transverse constraint imposed by BM and/or WM on HAZ.

The second issue in constructing a constitutive model for HAZ is to eliminate the effect of the transverse constraint from the measured stress–strain relationship. Yan et al. [5] proposed a possible solution by introducing a linear modification factor established in combined FEA and DIC analysis. The main idea is to reduce the measured true stress of HAZ. The beginning and the end of the modification factor correspond to the 0.2% proof stress yielding point and the necking point of HAZ, respectively. The modification factor is calibrated based on the inverse method. First, the measured HAZ constitutive model is directly used in FEA. Then, the FEA results are compared to the experimental results regarding the strain distribution on the specimen surface and the load–deformation relationship. The modification factor is then established by comparing the results. The modification factor can be calibrated in a trial-and-error procedure or by updating the material model in the so-called finite element model updated (FEMU) approach. The FEMU has been used to calibrate the mechanical [29,30] and thermal parameters [31] of metal materials. In the FEMU approach, a constitutive model with several assumed parameters is required as a starting point for the calibration procedure. The difference between the FEA and the experimental results is evaluated using a cost function. The target parameters are calibrated by minimizing the cost function.

Instead of the inverse method, the virtual fields method can be applied, as has been done to calibrate the heterogeneous constitutive model in a friction stir welded connection based on the tensile welded coupon tests [22,32]. According to these studies, the calibrated results show good agreement with the results of the uniform stress method [22], as the same assumptions, the plane stress condition and the different zones arranged in series in the thin coupon specimen, were made.

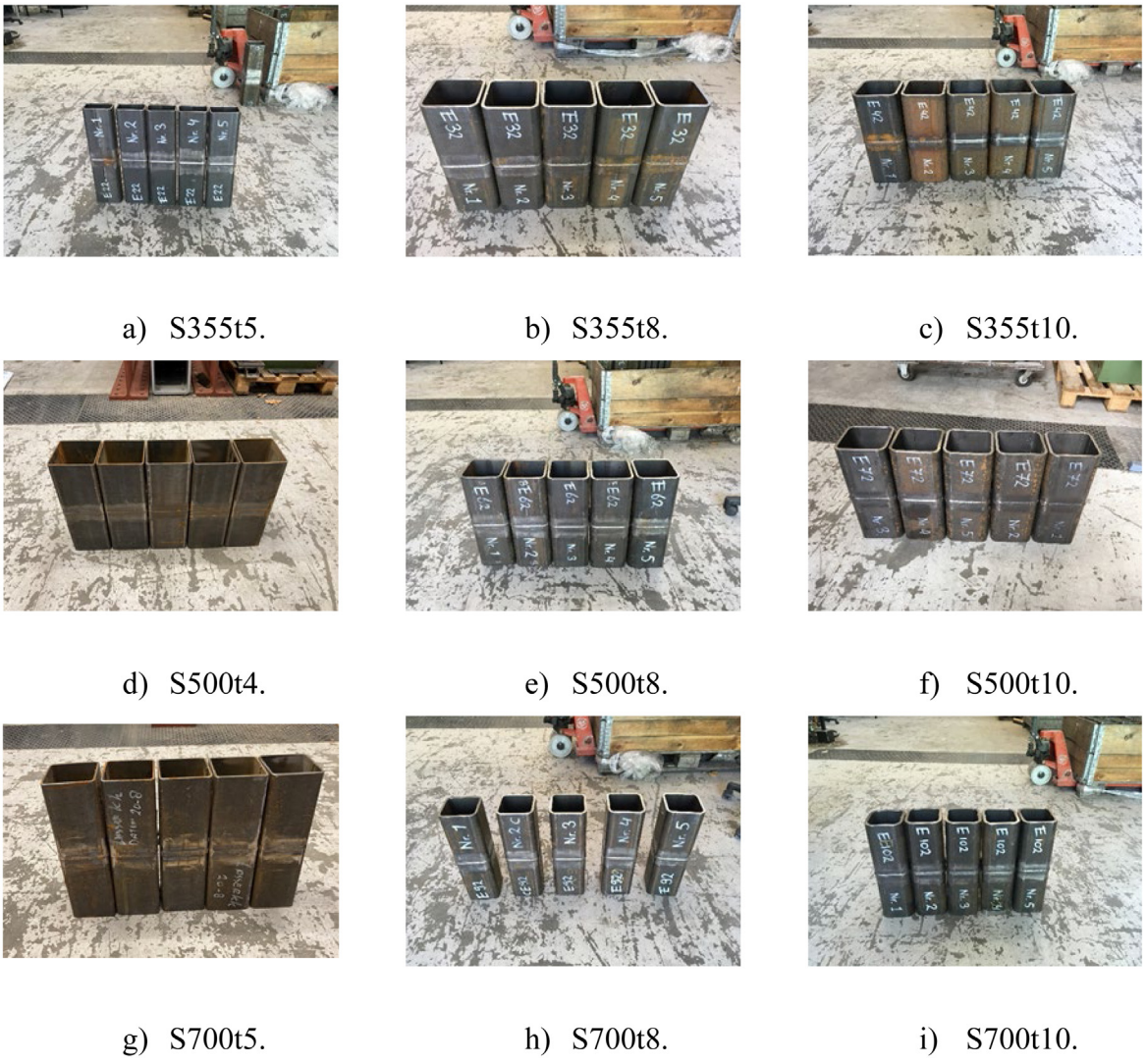

a) S355t5. b) S355t8. c) S355t10.

d) S500t4. e) S500t8. f) S500t10.

g) S700t5. h) S700t8. i) S700t10.

Fig. 1. Welded tubes.

In addition to the three direct approaches, attempts have been made to generate the HAZ constitutive model through two indirect experimental approaches. Firstly, the Vickers hardness test [4,17,33,34] can be used to predict the material yield and ultimate strength according to the empirical correlation between the material hardness and strength. The constitutive model parameters are determined based on the material strength derived from the material hardness. Another indirect approach evaluates the material constitutive model by the highest temperature measured during the welding process [35,36]. First, a thermal FEA is conducted to obtain the highest temperature of each element in a welded connection. Then, every element in the mechanical FEA is assigned a modified stress–strain relationship depending on the highest temperature. Finally, the material model is validated by comparing the load–deformation relationships obtained from the experiment and FEA.

3. Experimental and numerical tests

3.1. Test specimens

In this study, the stress–strain constitutive model of HAZ is investigated using nine profiles in three steel grades (S355J2H, S500MH, and S700MLH) and three thicknesses for each steel grade (4 or 5 mm, 8 mm, and 10 mm). Note that the S355 material has double steel grades S355J2H/S420MH. Five nominally identical tubular specimens for each profile were fabricated by welding two tube pieces together, as shown in Fig. 1. The profiles were square hollow sections (SHS) except for one rectangular hollow section (RHS) with a 5 mm thickness made of S355. The profile nominal dimensions, the thickness (t), and the outer corner radius (r) of the hollow sections are presented in Table 2. The code name of each profile consists of the steel grade and the nominal thickness. For example, S355t8 stands for the profile with S355 material and 8 mm nominal thickness. All tubes were manufactured by cold-forming thermo-mechanically rolled steel strips.

A single-bevel V groove was prepared on both tubes in a connection before welding, as shown in Fig. 2. Two bevelled tubes were manually

Table 2
Nominal dimensions of hollow sections and the position of coupon specimens.

Code name	Steel grade	Profile	t [mm]	r [mm]	d [mm]
S355t5		100 × 50 × 5	5	9	20
S355t8	S355	140 × 140 × 8	8	20	25
S355t10		160 × 160 × 10	10	25	35
S500t4		140 × 140 × 4	4	8.5	25
S500t8	S500	140 × 140 × 8	8	20	25
S500t10		160 × 160 × 10	10	25	35
S700t5		120 × 120 × 5	5	9	25
S700t8	S700	120 × 120 × 8	8	20	26
S700t10		120 × 120 × 10	10	25	17

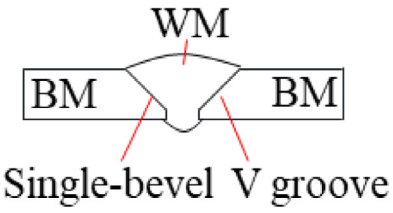

Fig. 2. The cross-section of the weld zone.

Table 3
Mechanical properties of filler metals.

Code-name	Yield strength [MPa]	Tensile strength [MPa]	A [%]
Carbofil 1	502	574	28
Union NiMoCr	720	780	17

welded by a full-penetration butt weld at a Dutch fabricator experienced in welding high-strength steels. The metal active gas (MAG) welding process was used according to the standard EN ISO 3834-2:2005 [37]. The minimum preheat temperature and the maximum interpass temperature were 20 °C and 200 °C, respectively. The heat input ranged between 1.0 kJ/mm and 1.4 kJ/mm. The shield gas contained 60% Ar, 30% He, and 10% CO_2. The filler metal Carbofil 1 was used for S355 tubes, whereas S500 and S700 tubes were welded by Union NiMoCr. The mechanical properties of filler metals provided by the fabricator are presented in Table 3. The chemical compositions of the base material and the filler metal given in the product certificate in weight percentage are shown in Table 4.

Three types of specimens were fabricated by water-jet cutting from the flat part of the wall opposite the side with the longitudinal weld, as depicted in Fig. 3. Conventional coupon specimens were extracted to obtain the BM stress–strain relationship. Two weld samples, cut from welded tubes (N1 and N2), were used to conduct the low-force Vickers hardness test (HV 0.5) and the microstructure observation. Welded coupon specimens with a butt weld in the middle were taken from the fabricated tube. Due to the weld reinforcement, the uniform stress assumption is not valid for HAZ, and the deformation of a distinct material zone (HAZ or WM) is not measurable using DIC. Hence, the welded coupon specimen was milled to a central thickness zone of 3 mm to have as "parallel" as possible boundaries of HAZ and "perpendicular" to the applied load. In addition, since the S355t10, S500t10, and S700t8 tubes were sufficiently wide, one additional row of coupon specimens was cut from the centre of the tube. Two extra welded specimens were not milled (weld reinforcement remained) to investigate the tensile behaviour of the complete weld zone. The two cutting schemes for the wide and narrow tubes are presented in Fig. 3. Note that the specimens, except for the central specimens, were symmetrically positioned around the central axis of the tube with a distance (d), as shown in Table 2.

The coupon specimen was designed with a 5.65 proportional coefficient following EN ISO 6892-1 [38]. The basic dimensions of the coupon specimen are presented in Fig. 4. The nominal width (b_0) and thickness (t_0) are summarized in Table 5, where the abbreviation 'No.' indicates the tube number. 'W' and 'UMW' stand for the milled and unmilled welded coupon specimens, respectively. The last letter, 'M', indicates that the specimen was taken from the centre row of the tube. Note there is no defined thickness for the unmilled welded coupon since the weld reinforcement results in a varying thickness. Besides, specimen S700t5WN2 is not available.

3.2. Metallurgical investigation

The weld sample of 40 mm, including an entire weld zone composed of BM, HAZ, and WM, was prepared for the metallurgical investigation and low-force Vickers hardness measurement. First, the sample was mounted in resin, allowing for convenient handling for subsequent operations. The sample was then sanded using SiC abrasive papers with 196 μm, 75 μm, 46 μm, 21.8 μm,15.2 μm, and 10 μm grit. Next, the sample was polished using MD/DP-Nap (1 μm cloth) to achieve a perfect mirror-like surface. Then, the 2% Nital solution was used to etch the prepared surface until the reflective surface became gloomy. The etching time was approximately 25 s. Finally, a Keyence VHX-7000 digital microscope was employed to observe the microstructure of the etched surface.

Since a mirror-like surface is preferred for the HV 0.5 hardness test, the polishing procedure was repeated after the microstructure observation. The standard HV 0.5 test [39,40] was conducted by an EMCO DuraScan 70 G5 automatic hardness tester. Fig. 5 shows the four indentation lines (in blue) for 8 mm and 10 mm thick samples, while three indentation lines were made on 4 mm and 5 mm thick samples. The parameter Y_i describes the distance from the top edge of the surface to each indentation line. An overview of the used Y_i is shown in Table 6. The orange lines in Fig. 5 indicate the HAZ boundary preliminarily identified by the observed microstructure. A 0.25 mm interval of indentation was used in regions including and close to HAZ, while a 1 mm interval was applied for the other regions. Note that the boundary identified by the microstructure is only used to determine approximate boundaries for the dense (0.25 mm interval) hardness test. Fig. 6 presents the employed samples for the metallurgical investigation.

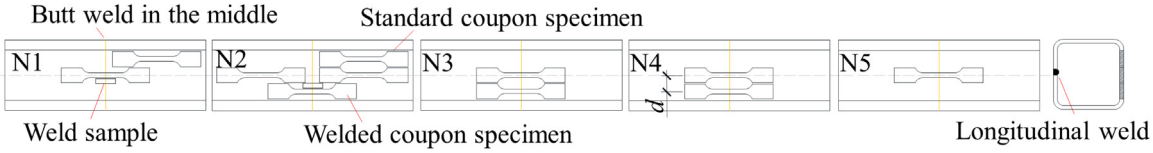

a) For wide profiles (S355t10, S500t10, S700t8).

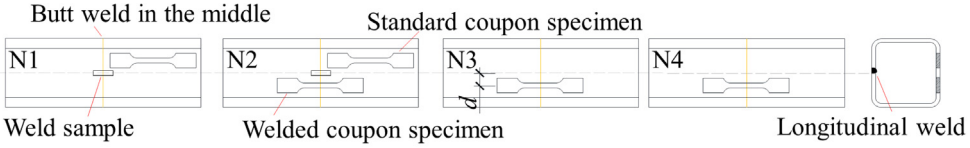

b) For narrow profiles (S355t5, S355t8, S500t4, S500t8, S700t5, S700t10).

Fig. 3. Specimen cutting scheme.

Table 4
Nominal chemical composition of the base material and the filler metal [wt%].

Code-name	C	Si	Mn	P	S	Cr	Ni	Cu	Mo	Ti	Al
S355t5	0.07	0.19	1.43	0.013	0.010	0.047	0.044	0.019	0.010	0.014	0.026
S355t8	0.07	0.19	1.42	0.012	0.006	0.051	0.037	0.015	0.008	0.015	0.037
S355t10	0.08	0.19	1.43	0.012	0.004	0.040	0.036	0.013	0.002	0.018	0.037
S500t4	0.06	0.19	1.20	0.011	0.004	0.047	0.036	0.015	0.003	0.002	0.036
S500t8	0.06	0.17	1.21	0.010	0.004	0.044	0.037	0.012	0.003	0.002	0.031
S500t10	0.05	0.17	1.19	0.009	0.003	0.037	0.035	0.012	0.005	0.002	0.030
S700t5	0.06	0.21	1.72	0.012	0.001	0.055	0.043	0.209	0.011	0.100	0.032
S700t8	0.05	0.19	1.81	0.011	0.002	0.041	0.037	0.014	0.005	0.110	0.036
S700t10	0.06	0.18	1.81	0.011	0.003	0.045	0.034	0.012	0.005	0.113	0.041
Carbofil 1	0.078	0.85	1.45	0.008	0.004	0.03	0.01	0.01	0.01	0.02	<0.01
Union NiMoCr	0.09	0.61	1.71	0.005	0.01	0.19	1.47	0.03	0.51	0.06	<0.01

Table 5
Nominal dimensions and annotation of coupon specimens.

Code-name	Standard [mm]			Milled welded [mm]			Unmilled welded [mm]	
	No.	t_0	b_0	No.	t_0	b_0	No.	b_0
S355t5	N1, N2	5	16	WN2, WN3, WN4	3	16	–	–
S355t8	N1, N2	8	10	WN2, WN3, WN4	3	10	–	–
S355t10	N1, N2 N2M1 N2M2	10	8	WN2, WN3, WN4 WN3M, WN4M	3	8	UMWN1M UMWN5M	8
S500t4	N1, N2	4	20	WN2, WN3, WN4	3	10	–	–
S500t8	N1, N2	8	10	WN2, WN3, WN4	3	10	–	–
S500t10	N1, N2 N2M1 N2M2	10	8	WN2, WN3, WN4 WN3M, WN4M	3	8	UMWN1M UMWN5M	8
S700t5	N1, N2	5	16	WN3, WN4	3	20	–	–
S700t8	N1, N2 N2M1 N2M2	8	10	WN2, WN3, WN4 WN3M, WN4M	3	10	UMWN1M UMWN5M	10
S700t10	N1, N2	10	8	WN2, WN3, WN4	3	8	–	–

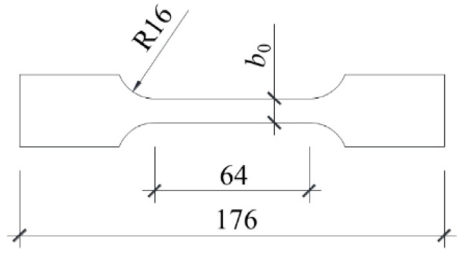

Fig. 4. Basic dimensions of coupon specimen.

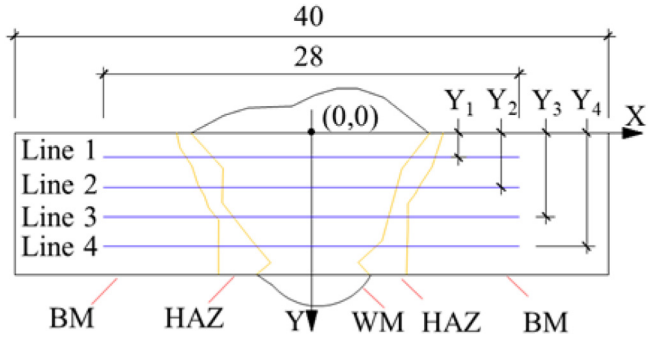

Fig. 5. Hardness testing scheme [mm].

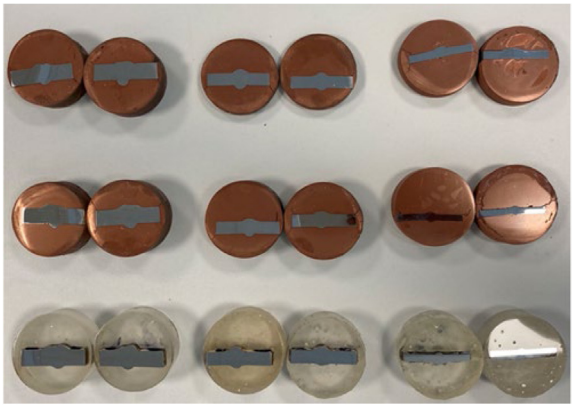

Fig. 6. Samples for the metallurgical investigation.

Table 6
The distance of the indentation line from the top edge [mm].

Code-name	Y_1	Y_2	Y_3	Y_4
S355t5, S500t4, S700t5	0.5	2.0	3.5	–
S355t8, S500t8, S700t8	1.5	3.0	5.0	6.5
S355t10, S500t10, S700t10	2.0	4.0	6.0	8.0

3.3. Tensile coupon tests

An Instron testing machine with 200 kN capacity was used to conduct the tensile coupon tests. Displacement-controlled loading with the rate of 0.01 mm/s was employed, according to the requirements in [38]. Since the proportional coefficient of the coupon specimen was 5.65, the initial gauge length for all coupon specimens was 50 mm. The coupon specimens for BM have an initial bow due to residual stresses generated in the tube during the cold-forming process. An extensometer was installed on the concave side of the specimen. In addition to the extensometer, a 3D DIC (ARAMIS) was employed to measure the deformation on the convex side, as shown in Fig. 7. The

Table 7
The determined width of HAZ and WM [mm].

Code-name	S355			S500			S700		
	t5WN4	t8WN2	t10WN2	t4WN3	t8WN2	t10WN2	t5WN3	t8WN2	t10WN2
HAZ_1	4	3	3	5	4	4	3	3	3.5
HAZ_2	3.5	3.5	4	4	4	3.5	3	3	2.5
WM	12	14	11.5	4	9	9	7.5	9.5	9

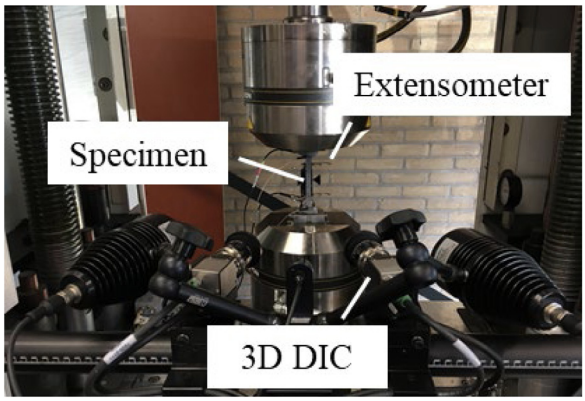

Fig. 7. Arrangement of measurements in the tensile test.

Fig. 8. Measured surface of the unmilled welded coupon specimen.

load–deformation relationships measured from the two devices were averaged to eliminate the effect of the initial bow [41]. The same measuring scheme applies to the milled welded coupon specimen. The DIC and the extensometer results were identical, as the milled coupon specimens were not curved. Hence, the testing results only from 3D DIC were used. For the unmilled coupon specimens, 3D DIC measured the deformation on the side with the complete weld zone, as shown in Fig. 8.

3.4. Finite element analysis (FEA)

In the case where BM and WM have higher yield and ultimate strength than HAZ, BM and WM may impose a transverse constraint on HAZ during the tensile test at the plastic stage, indicating that HAZ is under a biaxial tensile stress state instead of a uniaxial tensile stress state. According to the von Mises yield criterion (Eq. (1)), the measured yield strength (σ_y) would be higher if the stress in the x and z directions, resulting from the transverse constraint, was larger than 0.

$$\sigma_M = \sqrt{\frac{1}{2}\left[(\sigma_x - \sigma_y)^2 + (\sigma_y - \sigma_z)^2 + (\sigma_z - \sigma_x)^2 + 6\left(\tau_{xy}^2 + \tau_{yz}^2 + \tau_{zx}^2\right)\right]} \tag{1}$$

Consequently, the stress of the measured stress–strain relationship (the blue dashed line in Fig. 9(a)) is higher at a given strain level than what would be obtained if the stress state was uniaxial (the red dashed line in Fig. 9(a)). Yan et al. [5] proposed a method to eliminate the effect of the transverse constraint from the measured HAZ stress–strain relationship before necking. In this method, the measured stress is reduced using a linear modification function defined by two values (MF_1 and MF_2 in Fig. 9(a)). The same method is adopted in this paper to obtain the corrected HAZ constitutive model. Besides, the stress–strain relationships of BM and WM were taken from the normal BM coupon test and the milled welded coupon test, respectively. The measured stress–strain relationship of WM is extended using the Swift model [13] to generate the complete relationship, as WM did not fail.

The ABAQUS:2019 software package [42] was used to conduct FEA. Fig. 9(b) presents the 3D FE model for the milled welded coupon specimens, which is made based on measured dimensions. According to the hardness results from the central layer (referring to Line 2 and Line 3 in Fig. 5), a limited variation of the HAZ width through the thickness was found. Hence, a constant width for HAZ and WM is assumed in the FE model of the milled welded coupon specimen. Since the tensile test results of each profile show good consistency, only one test, deemed the most representative (the curve is in the 'middle' of all curves), was simulated to calibrate the values of MF_i. The widths of HAZ and WM were determined using the method proposed in [5,10], where the width was first derived based on the DIC result and then adjusted during the FEA calibration procedure. The results are presented in Table 7. Note that HAZ_1 and HAZ_2 represent the two HAZ zones besides WM.

A FE model containing the entire welded zone was created for unmilled coupon specimens to verify the constitutive model of HAZ, as shown in Fig. 9(c). The widths of the welded zone components are in accordance with the metallurgical results of weld samples, as illustrated in Section 4.1. Furthermore, to evaluate the effect of the transverse constraint in the width direction (the X direction in Fig. 9(b) and (c)) on the resistance of the welded connection, a quarter of welded SHS was created by extruding the weld cross-section of the S700 unmilled coupon specimen, as presented in Fig. 9(d). Note that no experimental tests were conducted on a complete welded SHS cross-section.

For the FE model of coupon specimens, the part within the 50 mm gauge length was meshed with 0.5 mm mesh size, while the remaining part uses a coarse mesh in the loading direction. The grip part of the specimen was not modelled to reduce the number of elements. For the FE model of the welded SHS, the 0.5 mm fine mesh was only used

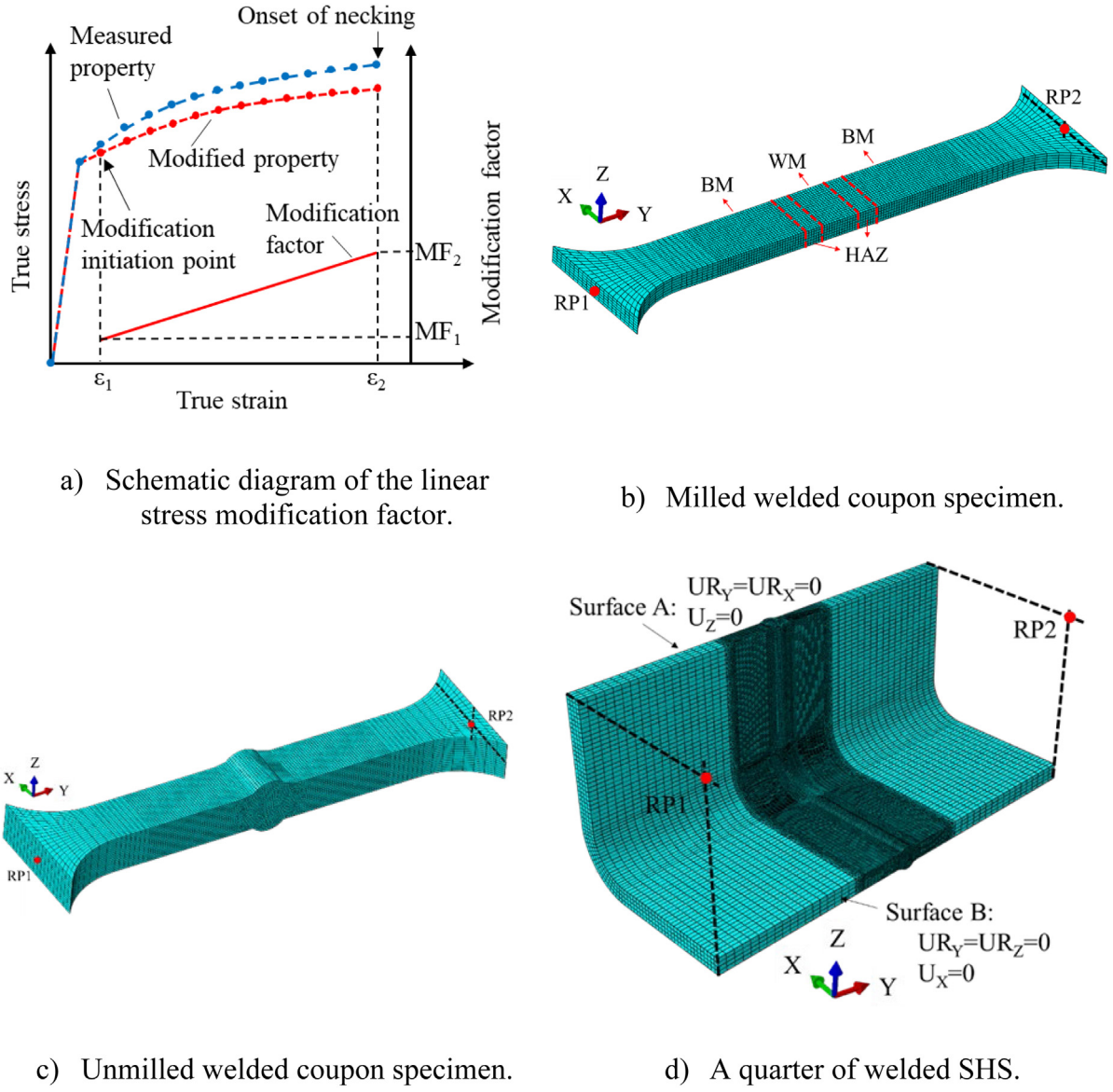

Fig. 9. Constitutive model and FE models.

for HAZ, WM, and 5 mm BM region close to the HAZ boundary on both sides. Two reference points (RP1 and RP2) were generated at the centre of two end surfaces or the centre of the entire SHS end surface. The end surface was controlled by the corresponding reference point in terms of all three translations and three rotations using the multi-point beam constraint (MPC beam). A positive displacement in the Y direction was applied at RP2 while the other degrees of freedom of the two reference points were fixed. Additionally, for the welded SHS, a symmetric boundary condition was applied on Surface A and B to model the entire SHS cross-section. Quasi-static analysis was performed using an explicit solver with a 100 s period and a 0.0001 s target time increment. Eight-node hexahedral solid elements with reduced integration (C3D8R) were used for the entire model.

3.5. A semi-empirical constitutive model for HAZ

All approaches introduced in Section 2 are rather complicated to implement in practice. A semi-empirical material model for HAZ based on the mechanical properties of BM would be ideal because it will significantly facilitate the advanced analysis of welded connections where HAZ is critical. Hence, a semi-empirical constitutive model for HAZ is proposed in this Section. The Swift model [13] (power law) is employed to generate the true stress-true strain relationship of HAZ. The expression of the original model is given in Eq. (2).

$$\sigma_t = A\left(\varepsilon_t + \varepsilon_0\right)^n \tag{2}$$

where σ_t and ε_t are the true stress and the true strain, respectively; A, ε_0, and n are the Swift parameters. Engineering stress σ_e and engineering strain ε_e can be converted to σ_t and ε_t for the constitutive model in the range before necking using Eq. (3). Hence, the σ_e - ε_e relationship following the Swift model is obtained by substituting Eq. (3) into Eq. (2), as shown in Eq. (4).

$$\begin{aligned} \sigma_t &= \sigma_e\left(1+\varepsilon_e\right) \\ \varepsilon_t &= \ln\left(1+\varepsilon_e\right) \end{aligned} \tag{3}$$

$$\sigma_e = \frac{A\left[\ln\left(1+\varepsilon_e\right)+\varepsilon_0\right]^n}{\left(1+\varepsilon_e\right)} \tag{4}$$

Table 8
HV 0.5 Hardness test results.

Code-name	N1						N2					
	Hardness			HAZ width [mm]			Hardness			HAZ width [mm]		
	BM_{ave}	HAZ_{min}	R	Max	Min	Ave	BM_{ave}	HAZ_{min}	R	Max	Min	Ave
S355t5	208	169	0.19	3.0	2.5	2.8	193	161	0.17	3.5	2.8	3.1
S355t8	180	153	0.15	4.0	2.3	3.0	179	156	0.13	3.5	2.5	2.9
S355t10	188	169	0.10	4.0	3.0	3.3	189	166	0.12	3.8	2.8	3.3
S500t4	221	176	0.20	4.3	2.3	3.4	220	178	0.19	4.5	2.0	3.6
S500t8	210	162	0.23	3.3	2.5	3.0	211	164	0.22	5.5	3.0	4.1
S500t10	222	187	0.16	4.5	2.0	3.2	213	183	0.14	3.5	2.5	3.2
S700t5	285	221	0.22	5.5	3.0	4.2	287	208	0.27	8.5(3.5)	2.0	4.7(3.0)
S700t8	277	191	0.31	5.0	2.8	3.5	281	208	0.26	3.3	2.5	2.8
S700t10	287	223	0.22	3.5	2.0	2.5	306	222	0.27	3.5	1.5	2.6

The three Swift parameters can be determined by three equations, as presented in Eq. (5). The first two equations are established by substituting the stress and strain at the yield strength point and the ultimate strength point into Eq. (4). In addition, the derivative of σ_e with respect to ε_e equals 0 at the ultimate strength point, which is the third equation.

$$\sigma_y = \frac{A\left[\ln\left(1+\varepsilon_y\right)+\varepsilon_0\right]^n}{\left(1+\varepsilon_y\right)}$$
$$\sigma_u = \frac{A\left[\ln\left(1+\varepsilon_u\right)+\varepsilon_0\right]^n}{\left(1+\varepsilon_u\right)} \quad (5)$$
$$\left.\frac{d\sigma_e}{d\varepsilon_e}\right|_{\varepsilon_e=\varepsilon_u} = -\frac{A\left[\ln\left(1+\varepsilon_u\right)+\varepsilon_0\right]^{n-1}\left(\ln\left(1+\varepsilon_u\right)+\varepsilon_0-n\right)}{\left(1+\varepsilon_u\right)^2} = 0$$

where the subscript 'y' and 'u' denote 'yield' and 'ultimate', respectively. In order to determine the Swift parameters for HAZ, engineering stress and engineering strain at the yield point and the ultimate point are required. Three reduction factors (RFs) are proposed to correlate the mechanical properties of BM and HAZ, as shown in Eq. (6). Note that the elongation at fracture, ε_f, of BM is correlated to the ultimate strain of HAZ. The reason is explained in Section 4.3.

$$\sigma_{y,HAZ} = RF_1 \times \sigma_{y,BM}$$
$$\sigma_{u,HAZ} = RF_2 \times \sigma_{u,BM} \quad (6)$$
$$\varepsilon_{u,HAZ} = RF_3 \times \varepsilon_{f,BM}$$

4. Test results

4.1. Metallurgical investigations

Table 8 presents the HV 0.5 hardness results of all weld samples. An example of the hardness characteristics is illustrated in Fig. 10. The minimum HAZ hardness is compared to the average BM hardness by the ratio R = 1 - $HAZ_{min}/BM_{ave,}$ which reflects the strength reduction in HAZ. The results from two samples for each profile show good agreement. The hardness difference increases as the steel grade increases. For S355 weld samples, the hardness of HAZ is 10% to 19% lower than BM. The varying range increases to 14%–23% for S500 weld samples and 22%–31% for S700. The hardness difference indicates that the strength reduction in HAZ is clearly greater in S700 than in S500 and S355. The hardness difference of the material investigated in this study is shown in Table 9, while the hardness difference of material found in the literature is presented in Table 1.

The hardness reduction in HAZ is plotted against the BM nominal yield strength in Fig. 11. The reference number is given for each result. The result of the current study is represented by [*]. It is worth mentioning again that the S355 material used in this study has

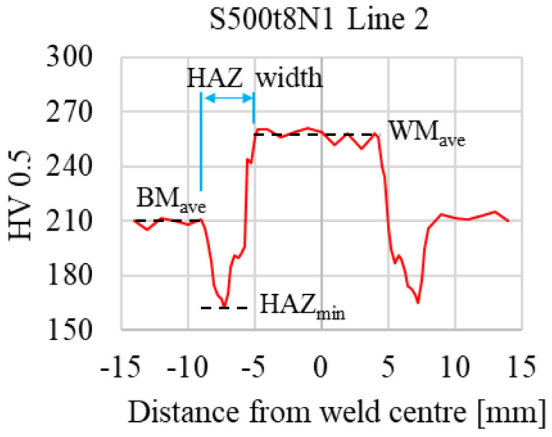

Fig. 10. An example of the hardness test result.

Table 9
Hardness reduction in HAZ.

Steel grade	Yield strength [MPa]	Processing method	Heat input [kJ/mm]	Hardness reduction in HAZ [%]
S355	355		1–1.4	10–19
S500	500	TMCP	1–1.4	14–23
S700	700		1–1.4	22–31

double steel grades S355J2H/S420MH. The hardness reduction in HAZ is more significant in the present study than in previous studies. One of the reasons is that the minimum HAZ hardness is compared to the average hardness of BM, while the average HAZ hardness is used in the literature. In addition, Pisarski and Dolby [7] found that the hardness degradation in HAZ is greater with an undermatching weld than with an overmatching weld, which might also explain the large hardness reduction of S700 HAZ (undermatching) in the present study. The matching type of the weld can be identified from the hardness contour plot (N2 samples) presented in Appendix. It can be seen that the WM hardness is roughly equal, higher, and lower than BM for S355, S500, and S700, respectively, indicating a matching, overmatching, and undermatching weld was made, correspondingly. Note that no correlation is observed between the HAZ hardness reduction and the plate thickness.

The measuring point with hardness below the average BM/WM hardness is considered to be the boundary between HAZ and BM/WM. The width of the HAZ is determined using these points, as shown in Fig. 10. The maximum, minimum, and average HAZ widths of 6 or 8 measurements (2 × 3 or 4 indentation lines) in each sample are presented in Table 8. The difference between the maximum and minimum HAZ width is not larger than 1 mm for half of the samples

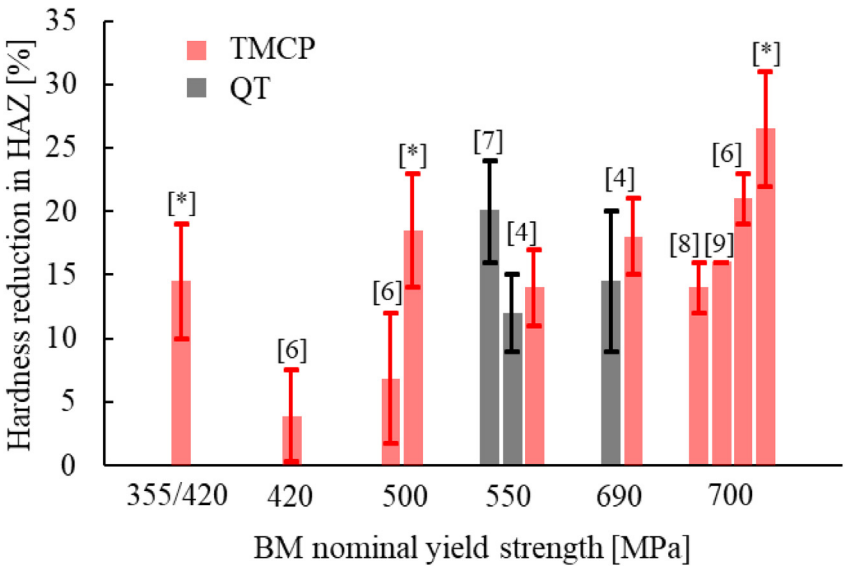

Fig. 11. Hardness reduction in HAZ vs. BM nominal yield strength.

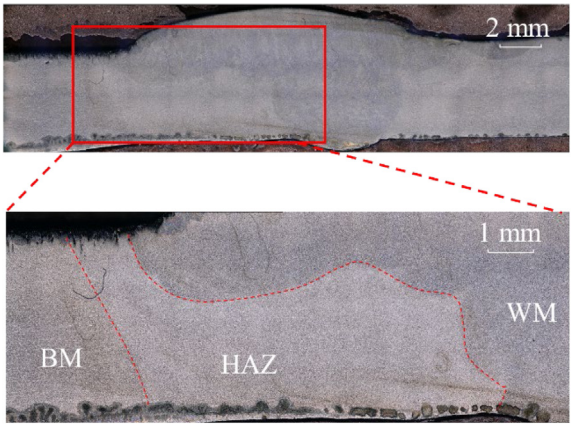

Fig. 12. Irregular weld (S700t5N2).

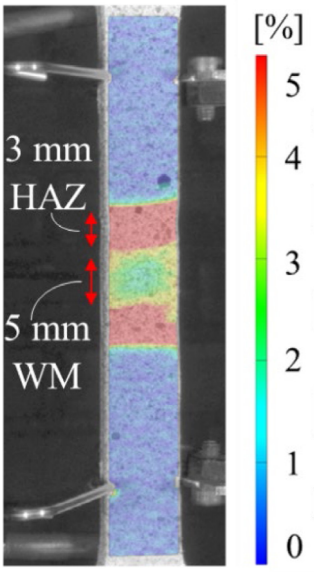

Fig. 13. Measuring range of virtual extensometers in DIC.

and not larger than 2 mm for 13 out of 18 samples. Considering all indentation lines, the majority (92%) of HAZ width varies between 2 mm and 4 mm. Since the HAZ width does not show a clear correlation to the BM thickness and the steel grade, an average 3.2 mm HAZ width is obtained including all HAZ but not the significantly large HAZ in S700t5N2 where an irregular shape of the weld was produced, as shown in Fig. 12. The result excluding the extreme wide HAZ is presented in the parentheses in Table 8.

Appendix shows the microstructure of the N2 sample for each profile. The microstructure of the material in the red dashed box is divided into four categories: (i) BM, (ii) the fine-grain heat-affected zone (FGHAZ), (iii) the coarse-grain heat-affected zone (CGHAZ), and (iv) WM. Typical microstructures of four regions are also presented. The boundary of these regions, represented by the red dashed line, is identified based on the distinct difference in the microstructure, which is also used to determine the regions with different intervals in the hardness test. It can be seen that the identified microstructure boundaries are in good agreement with the hardness results. The lowest hardness appears in FGHAZ.

4.2. Calibration of HAZ modification factors

The deformations of the HAZ and WM were obtained from the DIC results by placing virtual extensometers over each zone in milled welded coupon specimens. The metallurgical investigations show that the width of the HAZ is around 3 mm, and the width of the WM is usually larger than 7 mm. The fracture in HAZ aligns with the centre of the 3 mm extensometer, which measures the HAZ deformation. In the only two cases where the fracture does not appear in HAZ (S355t5WN3 and S500t10WN4 failed in BM), a 3 mm region with the highest strain at the beginning of the plastic stage is measured. The WM deformation is measured from the centre 5 mm of WM, smaller than the complete WM width (generally at least 7 mm) to avoid possible transverse constraints from HAZ. The measured stress–strain relationship of WM is also used in FEA for modelling the WM. An example that illustrates the measuring range of virtual extensometers (range of red arrow) is shown in Fig. 13.

Following the method proposed in [5], two values of MF_1 and MF_2 are calibrated for each type of profile and presented in Table 10. It is worth mentioning that the larger the strength difference between HAZ and WM/BM is, the higher MF is. No transverse constraint is observed at the yield point for S355 as MF_1 equals 0. Compared to

Table 10
The calibrated parameters.

Code	S355t5	S355t8	S355t10	S500t4	S500t8	S500t10	S700t5	S700t8	S700t10
MF_1 [%]	0	0	0	5	5	5	14	4	4
MF_2 [%]	4.5	4	5	7.5	3	0	10	8	6

Table 11
Mechanical properties of BM.

Code-name	No.	f_y [MPa]	f_u [MPa]	ε_f [%]	Code-name	No.	f_y [MPa]	f_u [MPa]	ε_f [%]
S355t5	N1	510	539	23.3	S355t10	N1	524	555	18.2
	N2	499	546	25.3		N2	507	537	26.6
S355t8	N1	504	535	26.9		N2M1	491	534	29.7
	N2	508	528	26.6		N2M2	514	531	27.9
S500t5	N1	565	635	22.5	S500t10	N1	568	607	21.2
	N2	566	638	21.0		N2	597	630	16.7
S500t8	N1	575	609	24.8		N2M1	560	595	24.3
	N2	585	614	24.9		N2M2	564	602	22.6
S700t5	N1	767	846	12.3	S700t8	N1	772	845	13.4
	N2	756	837	12.9		N2	784	857	13.8
S700t10	N1	812	907	12.2		N2M1	742	820	15.7
	N2	819	902	12.9		N2M2	737	811	12.7

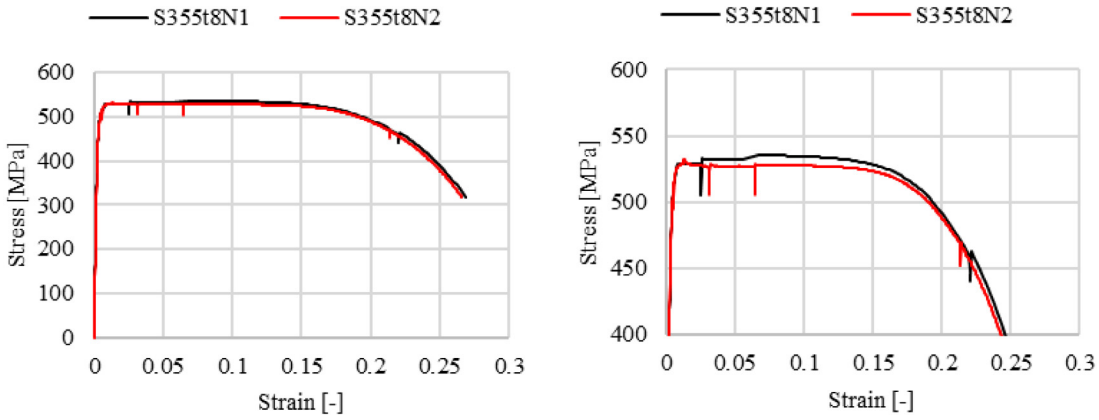

Fig. 14. Example of different ultimate strains.

S355 and S500, S700 has higher MFs, which aligns with the hardness results. Besides, MFs of S700t5 are significantly higher than S700t8 and S700t10. The reason is that the width of S700t5 was 20 mm while the other two specimens are not wider than 10 mm, which also implies that the width of the specimen may affect the extent of the transverse constraint.

4.3. Determination and validation of the HAZ constitutive parameters

The yield strength f_y (0.2% proof stress), the ultimate strength f_u, and the elongation at failure ε_f are determined for BM, as shown in Table 11.

The modification factors MF_1 and MF_2 were calibrated for one specimen of each profile. The calibrated MFs were used to calculate the modified yield strength f_y^* and the modified ultimate strength f_u^* for the other specimens extracted from the same profile, see Eq. (7). The measured strength, the modified strength, and the ultimate strain ε_u of HAZ are presented in Table 12 for all welded coupon specimens. Since the yield and ultimate strength of BM for each profile show good consistency, the average mechanical properties of BM are compared to HAZ to reveal the correlation between HAZ and BM. Note that the ultimate strength of HAZ in specimens S500t10WN2 and S500t10WN4 is higher than BM, as the average ultimate strength is used for BM. Fig. 14 presents the engineering stress–strain relationship of the S355t8 profile. It can be seen that the ultimate strain (corresponding to the ultimate strength) of the two specimens differ significantly (0.015 for S355t8N1 and 0.081 for S355t8N2), although the two curves are almost identical from a global perspective. Hence, the elongation at failure ε_f, which can also reflect the ductility of the material, is used to compare with the ultimate strain of HAZ.

$$f_y^* = f_y \times \left(1 - \frac{MF_1}{100}\right)$$
$$f_u^* = f_u \times \left(1 - \frac{MF_2}{100}\right) \quad (7)$$

The yield strength ratio $f_{y,HAZ}^*/f_{y,BM}$, the ultimate strength ratio $f_{u,HAZ}^*/f_{u,BM}$, and the strain ratio $\varepsilon_{u,HAZ}/\varepsilon_{f,BM}$ of all tested welded coupon specimens are presented in Table 12. The ratios of S355 and S500 vary in a very similar range, where the yield strength and the ultimate strength of HAZ are on average 13% and 4% lower than BM, respectively. A significant strength reduction in HAZ is observed

Table 12
Comparison of HAZ and BM.

Specimen	$f_{y,BM}$ [MPa]	$f_{y,HAZ}$ [MPa]	$f^*_{y,HAZ}$ [MPa]	$\frac{f^*_{y,HAZ}}{f_{y,BM}}$	$f_{u,BM}$ [MPa]	$f_{u,HAZ}$ [MPa]	$f^*_{u,HAZ}$ [MPa]	$\frac{f^*_{u,HAZ}}{f_{u,BM}}$	$\varepsilon_{f,BM}$ [%]	$\varepsilon_{u,HAZ}$ [%]	$\frac{\varepsilon_{u,HAZ}}{\varepsilon_{f,BM}}$
S355t5WN2		453	453	0.90		561	533	0.98		18.5	0.76
S355t5WN3	505	430	430	0.85	543	549	521	0.96	24.3	16.6	0.68
S355t5WN4		431	431	0.85		545	518	0.95		20.0	0.82
S355t8WN2		465	465	0.92		545	523	0.99		23.0	0.86
S355t8WN3	506	451	451	0.89	531	535	514	0.97	26.8	16.8	0.63
S355t8WN4		454	454	0.90		538	516	0.97		16.7	0.62
S355t10WN2		474	474	0.93		569	541	1.00		16.2	0.63
S355t10WN3		419	419	0.82		537	510	0.95		18.8	0.73
S355t10WN3M	509	426	426	0.84	539	524	498	0.92	25.6	20.6	0.80
S355t10WN4		441	441	0.87		541	514	0.95		17.1	0.67
S355t10WN4M		430	430	0.84		535	508	0.94		18.6	0.73
S500t4WN2		522	496	0.88		643	596	0.94		15.5	0.71
S500t4WN3	566	518	492	0.87	637	645	598	0.94	21.8	14.9	0.69
S500t4WN4		522	496	0.88		638	587	0.92		16.2	0.74
S500t8WN2		531	504	0.87		606	588	0.96		17.0	0.68
S500t8WN3	580	504	479	0.83	612	577	560	0.92	24.9	16.0	0.64
S500t8WN4		520	494	0.85		586	573	0.94		13.2	0.53
S500t10WN2		564	536	0.94		632	632	1.04		13.3	0.63
S500t10WN3		513	487	0.85		593	593	0.98		19.2	0.91
S500t10WN3M	572	515	489	0.85	609	593	593	0.97	21.2	13.9	0.66
S500t10WN4		545	518	0.91		615	615	1.01		10.4	0.49
S500t10WN4M		532	506	0.88		610	610	1.00		12.7	0.60
S700t5WN2		–	–	–		–	–	–		–	–
S700t5WN3	762	585	503	0.66	841	795	716	0.85	12.6	14.7	1.17
S700t5WN4		673	579	0.76		793	713	0.85		10.1	0.80
S700t8WN2		589	566	0.75		712	655	0.79		11.7	0.84
S700t8WN3		608	583	0.77		717	660	0.79		12.3	0.88
S700t8WN3M	759	632	607	0.80	833	726	668	0.80	13.9	11.3	0.81
S700t8WN4		606	581	0.77		709	654	0.79		12.7	0.91
S700t8WN4M		574	551	0.73		707	650	0.78		11.1	0.80
S700t10WN2		656	630	0.77		780	733	0.81		11.5	0.92
S700t10WN3	816	696	668	0.82	904	789	741	0.82	12.6	13.9	1.11
S700t10WN4		701	673	0.83		798	750	0.83		9.2	0.73

in the S700 material, as the average yield strength ratio and the ultimate strength ratio are 0.76 and 0.81, respectively. It is worth mentioning that the ultimate strength reduction in HAZ varies in a very similar range with a maximum 4% difference compared to another research [4], where the HAZ ultimate strength is predicted based on the hardness result. The average strain ratio of S355, S500, and S700 are 0.72, 0.66 and 0.84, respectively. Besides, there is no clear relationship between the ratios and the thickness of the original profile for all materials.

The yield strength ratio, the ultimate strength ratio, and the strain ratio of most specimens (at least 9 out of 11 or 10) are not smaller than 0.84, 0.94, and 0.6 for S355 and S500, and not smaller than 0.7, 0.79, and 0.8 for S700, respectively. Hence, a set of rather conservative reduction factors (RFs), introduced in Eq. (6), are determined for each steel grade, as presented in Table 13. Based on the BM average mechanical properties and the determined RFs, the three Swift parameters are derived for three profiles (S355t10, S500t10, S700t8); see Table 13. The derived constitutive model of HAZ is further validated by the FEA of unmilled welded coupon tests. It is worth mentioning that the proposed HAZ constitutive model is valid for welds using the same welding method and welding parameters presented. The heat input is in a range of 1.0 kJ/mm to 1.4 kJ/mm.

Fig. 15 presents the load–deformation relationship of the unmilled welded coupon tests. The results of the two specimens for each profile are in good agreement. The fracture of S355t10 and S500t10 specimens shifts from HAZ in the milled welded coupon specimen to BM in the unmilled welded coupon specimen, while the S700t8 specimen failed in HAZ in both the milled and unmilled specimens, as shown in Fig. 16. Hence, the deformation capacity of S355t10 and S500t10 specimens

Table 13
Determined constitutive parameters for HAZ.

Steel grade	RF_1	RF_2	RF_3	Code-name	A	n	ε_0
S355	0.85	0.95	0.6	S355t10	797	0.167	0.0236
S500	0.85	0.95	0.6	S500t10	851	0.132	0.0122
S700	0.7	0.8	0.8	S700t8	942	0.108	0.0024

are significantly higher than S700t8 specimens. Note that the low deformation capacity of S700t8 specimens is not attributed to the lower ductility of S700 BM compared to S355 BM and S500 BM, as a limited strain (around yielding) was observed in BM. The lower deformation capacity of S700t8 specimens is also demonstrated by the fact that the modified ultimate strength of HAZ is smaller than the yield strength of BM, implying that the HAZ fails before yielding in BM. Besides, with an increasing measuring length, the deformation capacity increase of S355 and S500 specimens would be even larger than S700 specimens since the S355 and S500 specimens have a significantly higher strain in BM than the S700 specimen.

The shift in the fracture position implies that the transverse constraint in the thickness direction, especially resulting from the reinforcement of WM, contributes to the HAZ resistance. In addition, the equivalent ultimate strength (the total load divided by the cross-sectional area of the parallel part) of the S700t8 unmilled specimens is on average 769 MPa, which is 8% higher than the average ultimate strength of S700t8 milled specimens.

The FE results are compared to the experiments in Fig. 15. It can be seen that the tensile behaviour of the unmilled coupon specimen is well predicted using the semi-empirical HAZ constitutive model based on

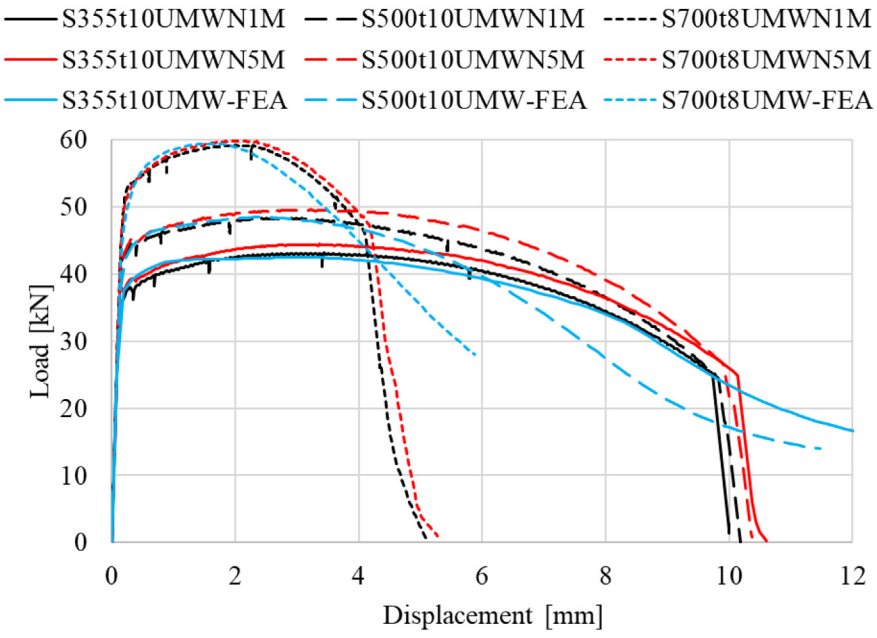

Fig. 15. Load–displacement relationship of unmilled welded coupon specimens.

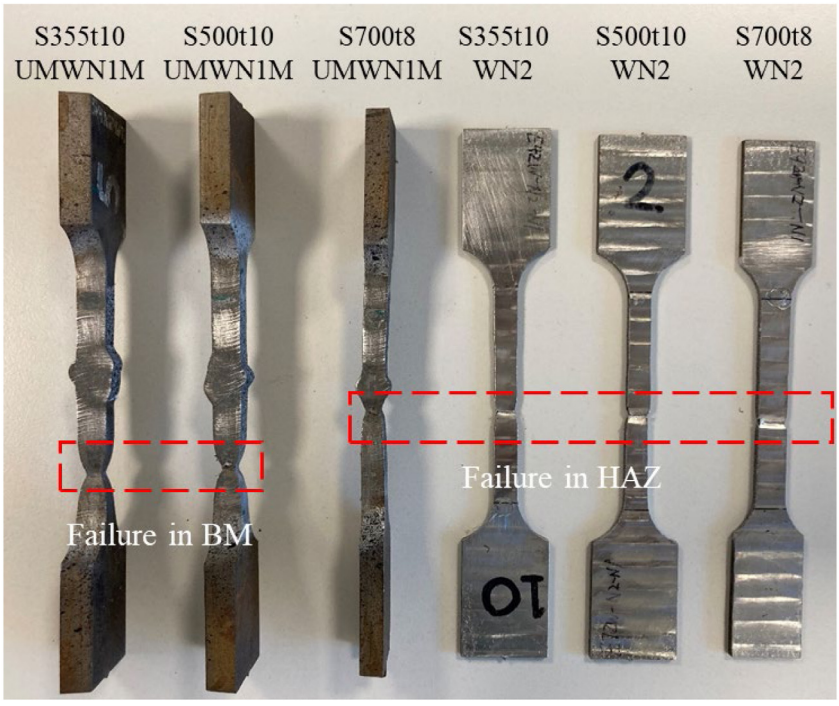

Fig. 16. Failure of milled and unmilled welded coupon specimens.

the BM mechanical properties and corresponding RFs. Comparing the FE ultimate resistance to the experiment, the maximum deviation is less than 3%. In addition, the FE models successfully predicted the necking position in experiments (HAZ for S700 and BM for S355 and S500). Hence, it is concluded that the derived HAZ equivalent constitutive model can effectively represent the HAZ mechanical properties.

4.4. Effect of transverse constraint on the HAZ resistance

The effect of transverse constraint in the width direction on the resistance of the welded connection is evaluated in this section based on the one-quarter welded SHS FE model (see Fig. 9(d)). Note that the width direction of the specimen refers to the X direction of the milled and unmilled specimen and the X/Z direction of the SHS model, as shown in Fig. 9. S355 and S500 unmilled welded coupon specimens failed in BM, indicating the failure of SHS connections using S355 and S500 materials would be in BM as well. Therefore, the increasing effect of the transverse constraint in the width direction cannot be evaluated by testing S355 and S500 materials in the welded SHS connection. Hence, only the calibrated HAZ stress–strain relationship of S700t8 was used to further study the one-quarter welded SHS FE model. Although the failure still occurs in HAZ, the HAZ equivalent ultimate strength (the total load divided by the SHS cross-section area) significantly increases to $f_{u,HAZ,SHS} = 848$ MPa, which is almost identical to the ultimate strength (880 MPa) of the model using the BM stress–strain relationship for all zones, as shown in Fig. 17.

The verified MF_2 for S700t8 indicates that the transverse constraint in the width direction of the milled coupon specimen results in an 8% strength enhancement in HAZ at the ultimate state ($f^*_{u,HAZ} = 0.92 \times f_{u,HAZ,milled}$). Comparing the average ultimate strength (S700t8) of the unmilled welded coupon specimens to the milled welded coupon specimens, the ultimate strength increases by 8% due to the transverse constraint in the thickness direction ($f_{u,HAZ,unmilled} = 1.08 \times f_{u,HAZ,milled}$). Therefore, the BM and WM of a full-thickness weld connection may enhance the HAZ ultimate strength (without the transverse constraint) by 17% ($f_{u,HAZ,unmilled} = 1.08/0.92 \times f^*_{u,HAZ}$). Furthermore, the enhancement would be even higher if a wider specimen is considered, such as the welded SHS connection, where the HAZ ultimate strength is improved by 29% compared to the HAZ ultimate strength ($f_{u,HAZ,SHS} = 1.29 \times f^*_{u,HAZ}$), see Fig. 17.

5. Conclusions

In this paper, the equivalent mechanical properties of the heat-affected zone (HAZ) are investigated using a semi-empirical methodology. HAZ is considered a homogeneous material, with no distinction of different volumetric fractions of microstructures. The following conclusions are drawn for welds using the same welding method and welding parameters presented:

1. For S355 and S500, the yield strength and the ultimate strength of HAZ are on average 13% and 4% lower than the base material (BM). The S700 HAZ yield and ultimate strength degradation are 24% and 19% compared to BM, respectively. The ultimate strain of S355, S500, and S700 HAZ are 0.72, 0.66 and 0.84 times the BM elongation at fracture, respectively.
2. Three reduction factors (RFs) are proposed to correlate the mechanical properties of BM and HAZ. The proposed RFs for the yield strength, the ultimate strength, and the ultimate strain are 0.85, 0.95, 0.6 for S355 and S500, and 0.7, 0.8, 0.8 for S700, respectively. The derived HAZ mechanical properties are used to generate the stress–strain relationship based on the Swift model. The derived HAZ constitutive model for each steel grade is successfully validated against the experiments.

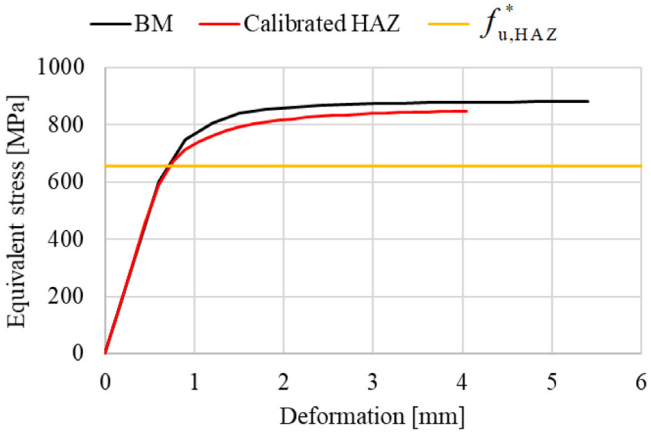

Fig. 17. Equivalent stress–deformation relationship of welded SHS.

3. The modification factors (MF_1 and MF_2) account for the transverse constraint imposed by BM and the weld metal (WM) on HAZ, as the transverse constraint increases the resistance of HAZ. In an S700t8 welded connection, the ultimate strength of HAZ in the unmilled welded coupon specimen is 17% higher than the modified ultimate strength of HAZ. The difference is increased to 29% due to the higher constraint in the case of the complete butt-welded SHS.
4. The low-force Vickers hardness test results show that the majority (92%) of HAZ has a width ranging from 2 mm to 4 mm. The HAZ width does not show any correlation to the steel grade and the plate thickness. The mean value of HAZ width is 3.2 mm.

For future studies, the stress–strain relationship of HAZ should be investigated considering different heat inputs, cooling times ($t_{5/8}$), and types of the base material. And the validated range of the proposed semi-empirical HAZ constitutive model could be expanded.

CRediT authorship contribution statement

Rui Yan: Writing – review & editing, Writing – original draft, Visualization, Validation, Software, Methodology, Investigation, Formal analysis, Data curation, Conceptualization. **Kristo Mela:** Writing – review & editing, Resources, Project administration, Funding acquisition. **Fei Yang:** Writing – review & editing, Methodology. **Hagar El Bamby:** Data curation. **Milan Veljkovic:** Writing – review & editing, Supervision, Resources, Funding acquisition.

Declaration of competing interest

The authors declare that they have no known competing financial interests or personal relationships that could have appeared to influence the work reported in this paper.

Data availability

Data will be made available on request.

Acknowledgement

The authors would like to thank the company SSAB Europe for the financial support.

Appendix. microstructure observation (FGHAZ: fine-grain heat-affected zone; CGHAZ: Coarse-grain heat-affected zone)

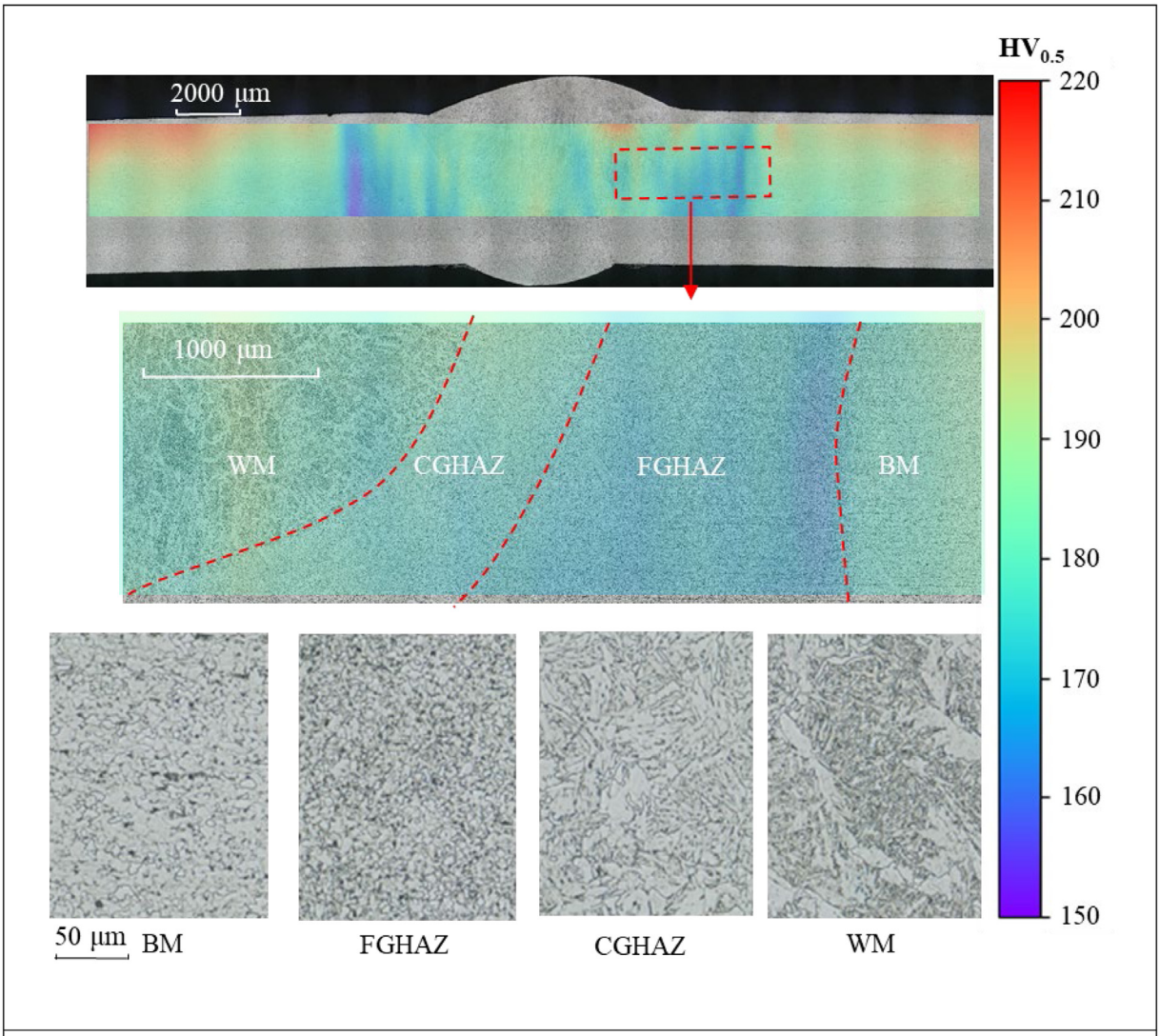

a) S355t5N2.

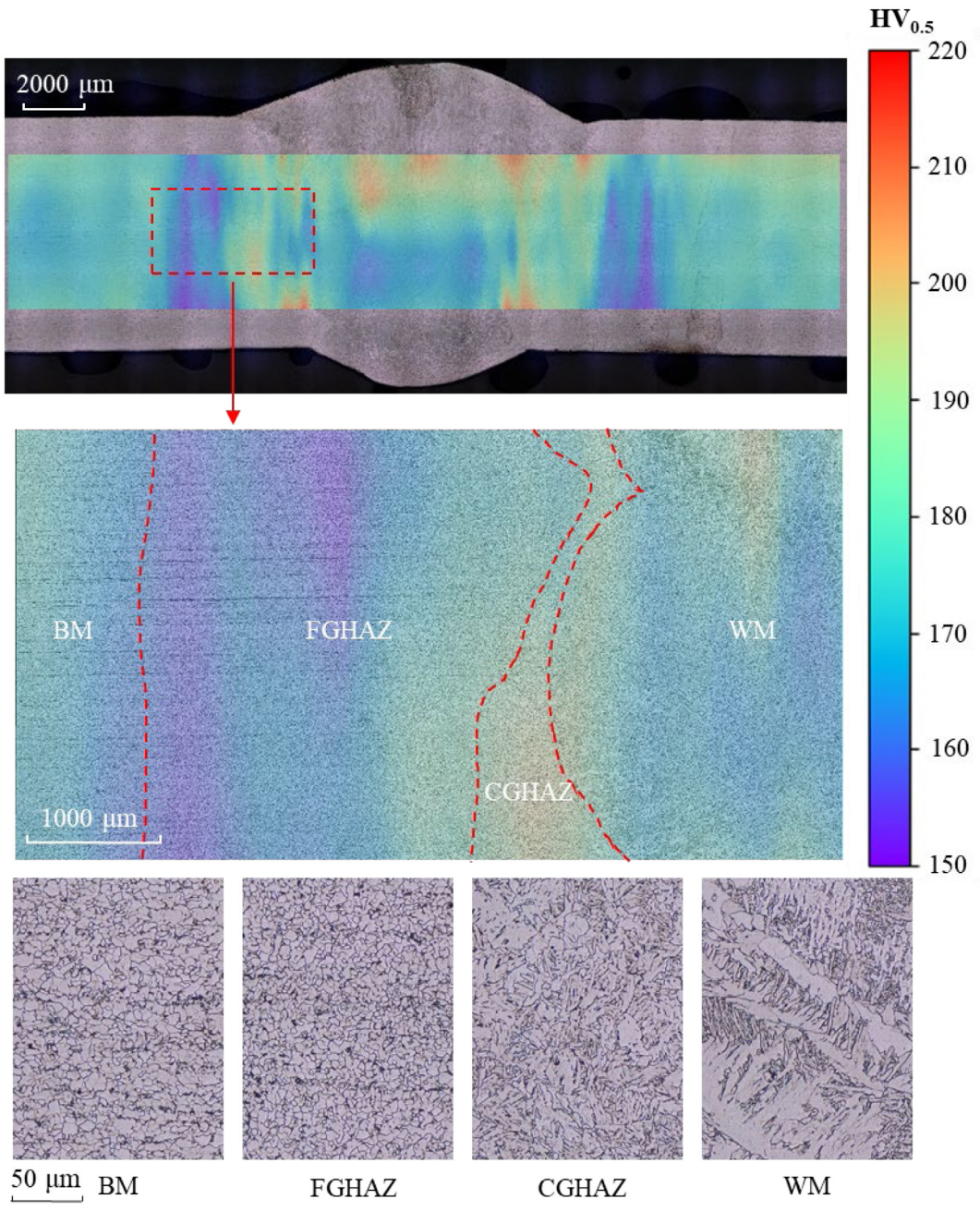
HV0.5
220
210
200
190
180
170
160
150
2000 µm
BM
FGHAZ
CGHAZ
WM
1000 µm
50 µm
BM
FGHAZ
CGHAZ
WM

b) S355t8N2.

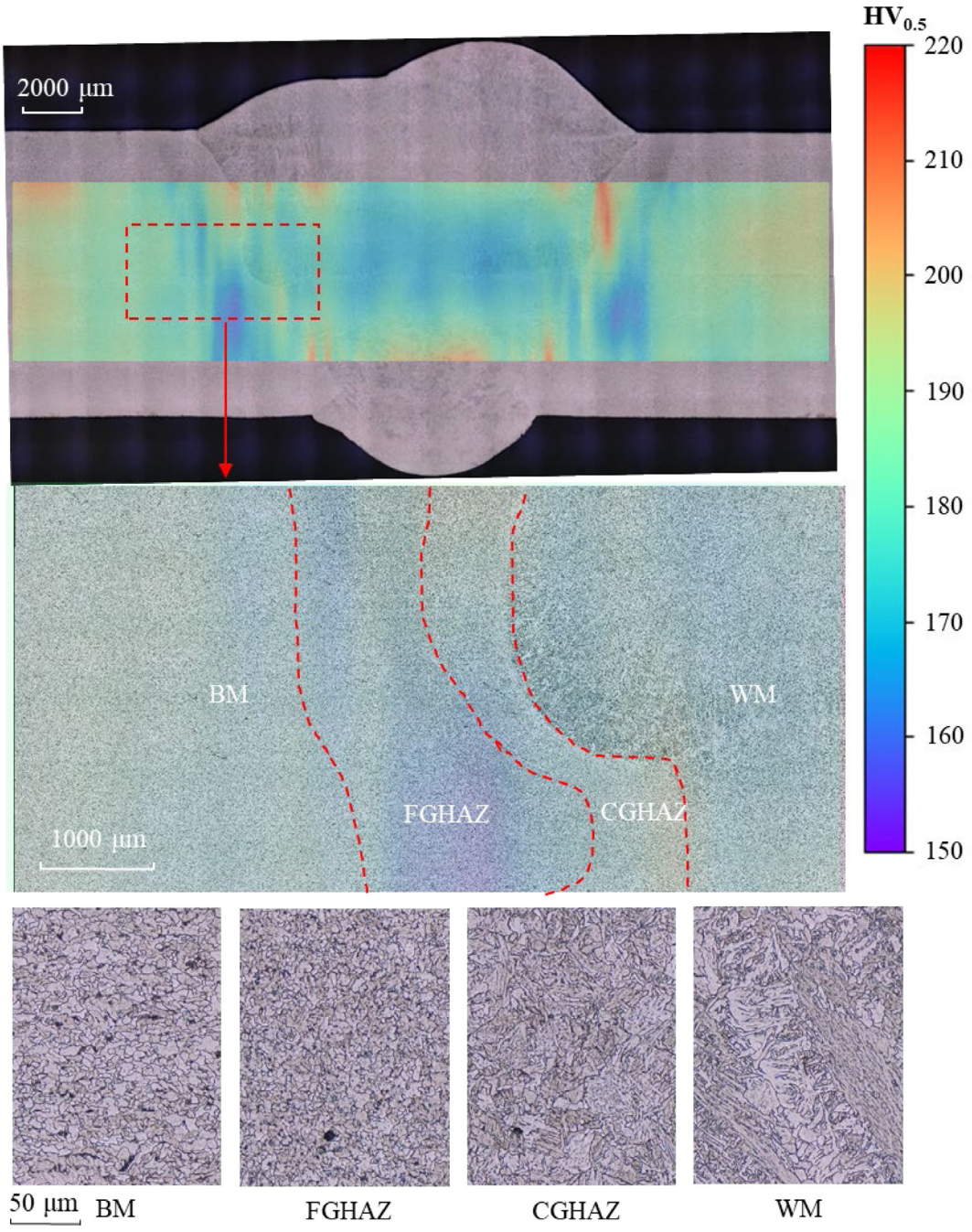
HV0.5
220
210
200
190
180
170
160
150
2000 µm
BM
WM
FGHAZ
CGHAZ
1000 µm
50 µm
BM
FGHAZ
CGHAZ
WM

c) S355t10N2.

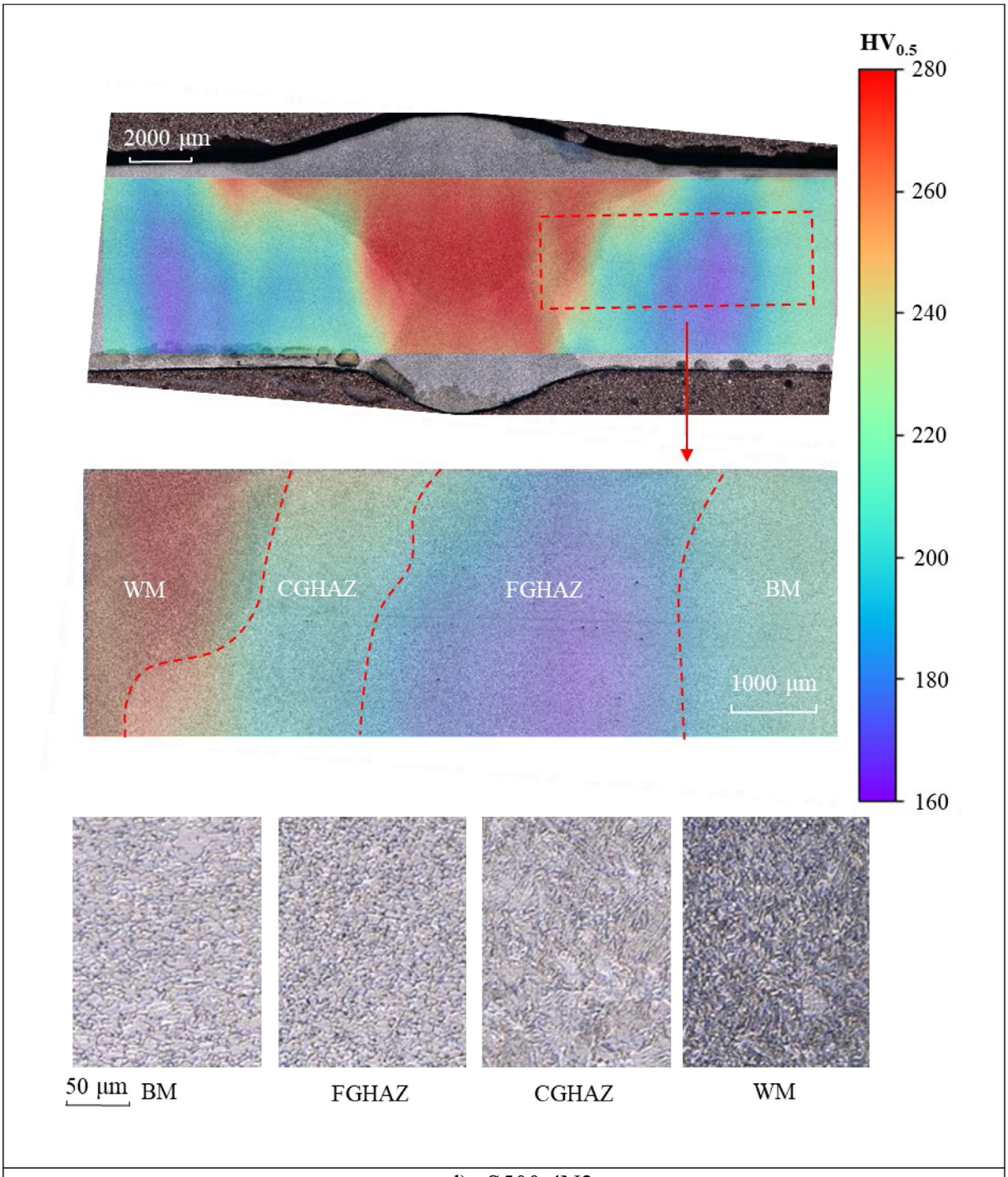
HV0.5
280
260
240
220
200
180
160
2000 µm
WM
CGHAZ
FGHAZ
BM
1000 µm
50 µm
BM
FGHAZ
CGHAZ
WM

d) S500t4N2.

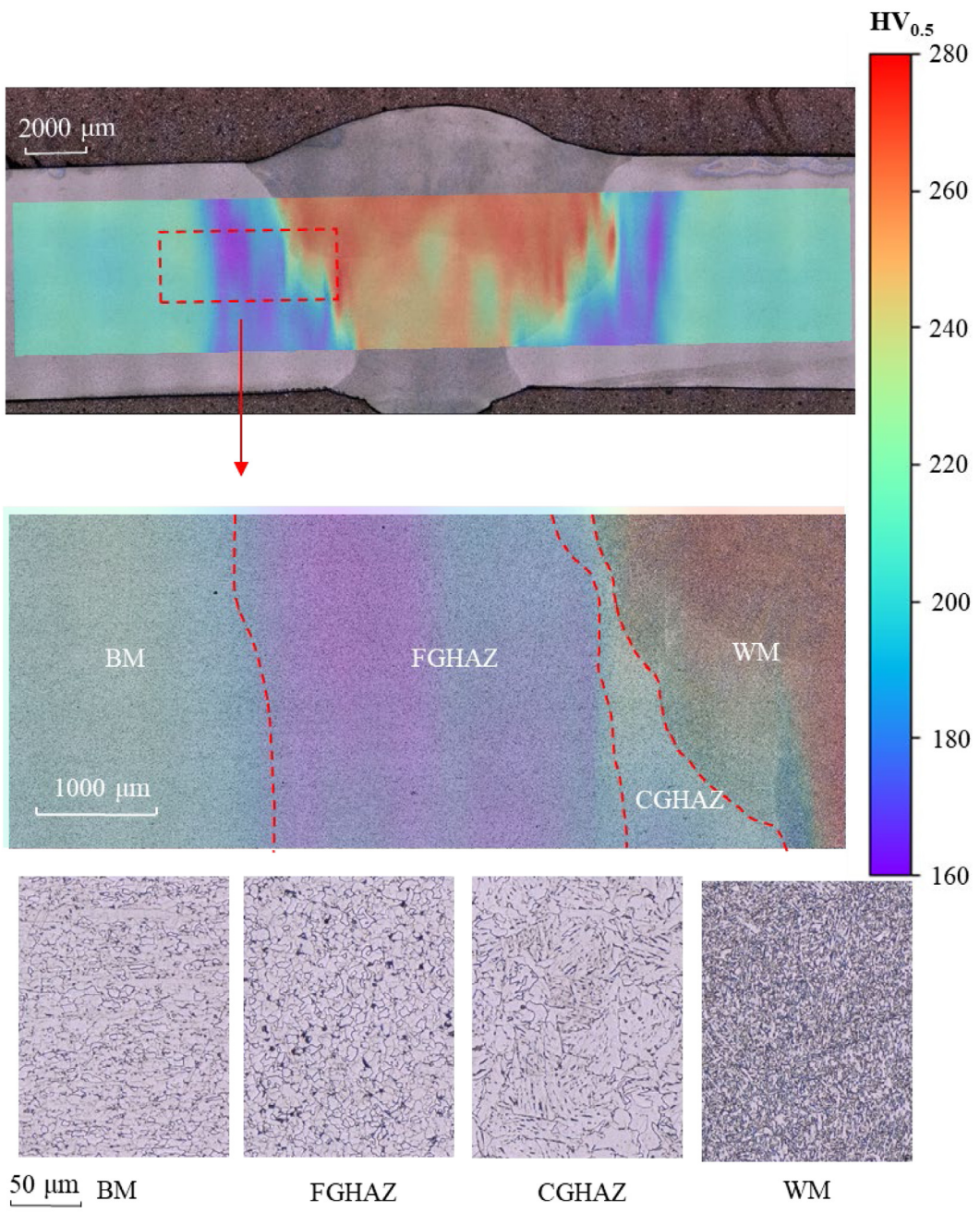
HV0.5
280
260
240
220
200
180
160
2000 µm
BM
FGHAZ
WM
1000 µm
CGHAZ
50 µm
BM
FGHAZ
CGHAZ
WM

e) S500t8N2.

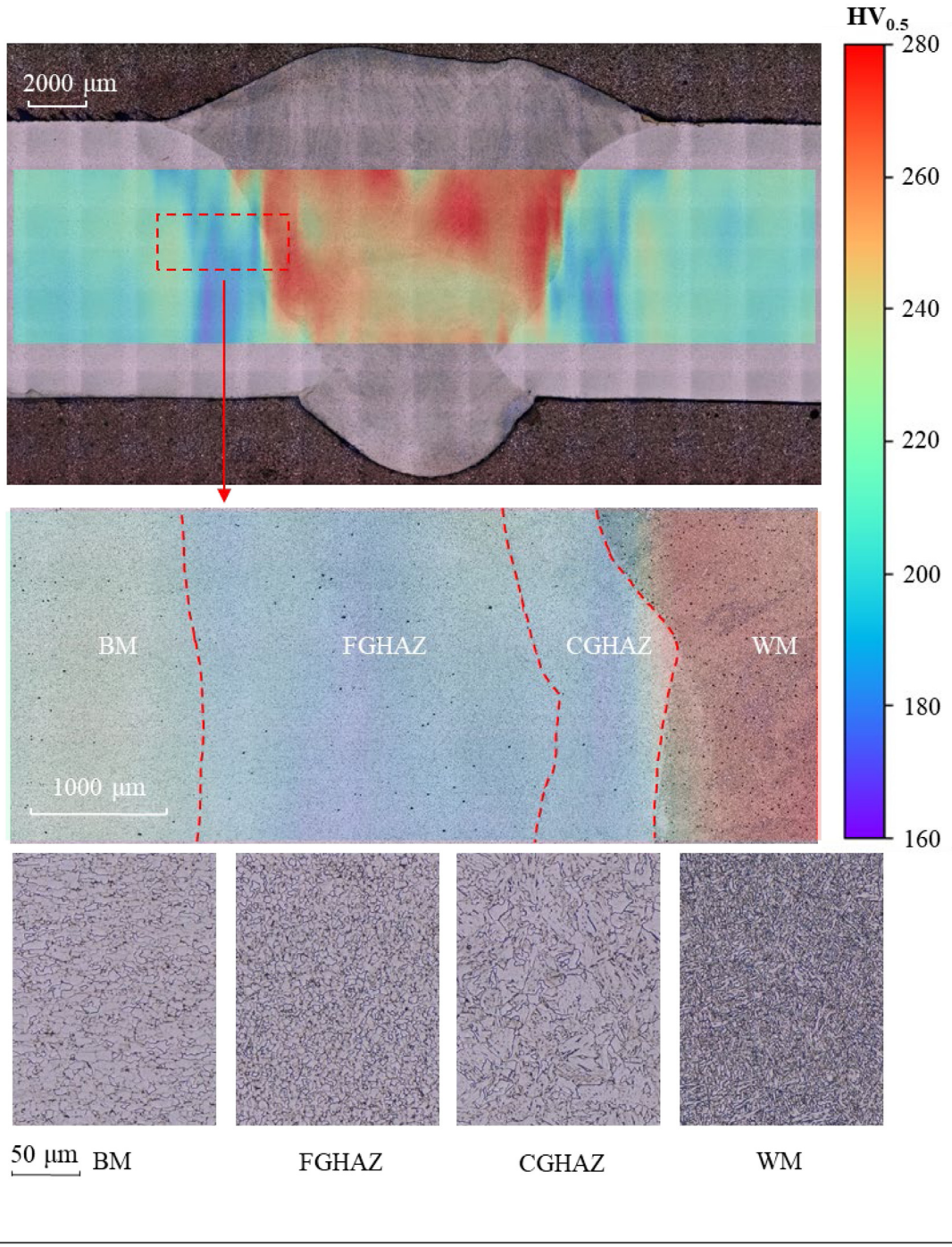
HV0.5
280
260
240
220
200
180
160
2000 µm
BM
FGHAZ
CGHAZ
WM
1000 µm
50 µm
BM
FGHAZ
CGHAZ
WM

f) S500t10N2.

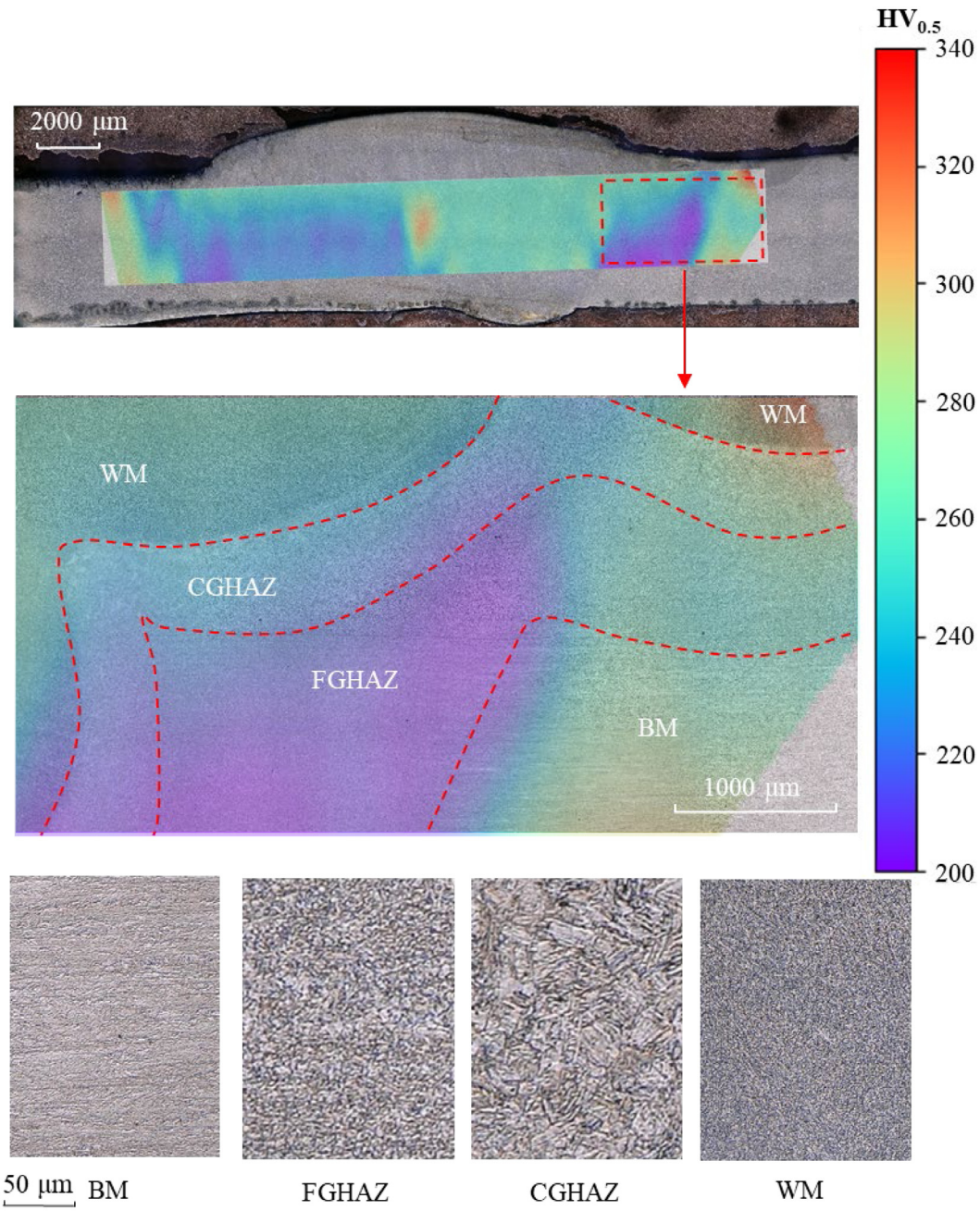
HV0.5
340
320
300
280
260
240
220
200
2000 µm
WM
WM
CGHAZ
FGHAZ
BM
1000 µm
50 µm BM
FGHAZ
CGHAZ
WM

g) S700t5N2.

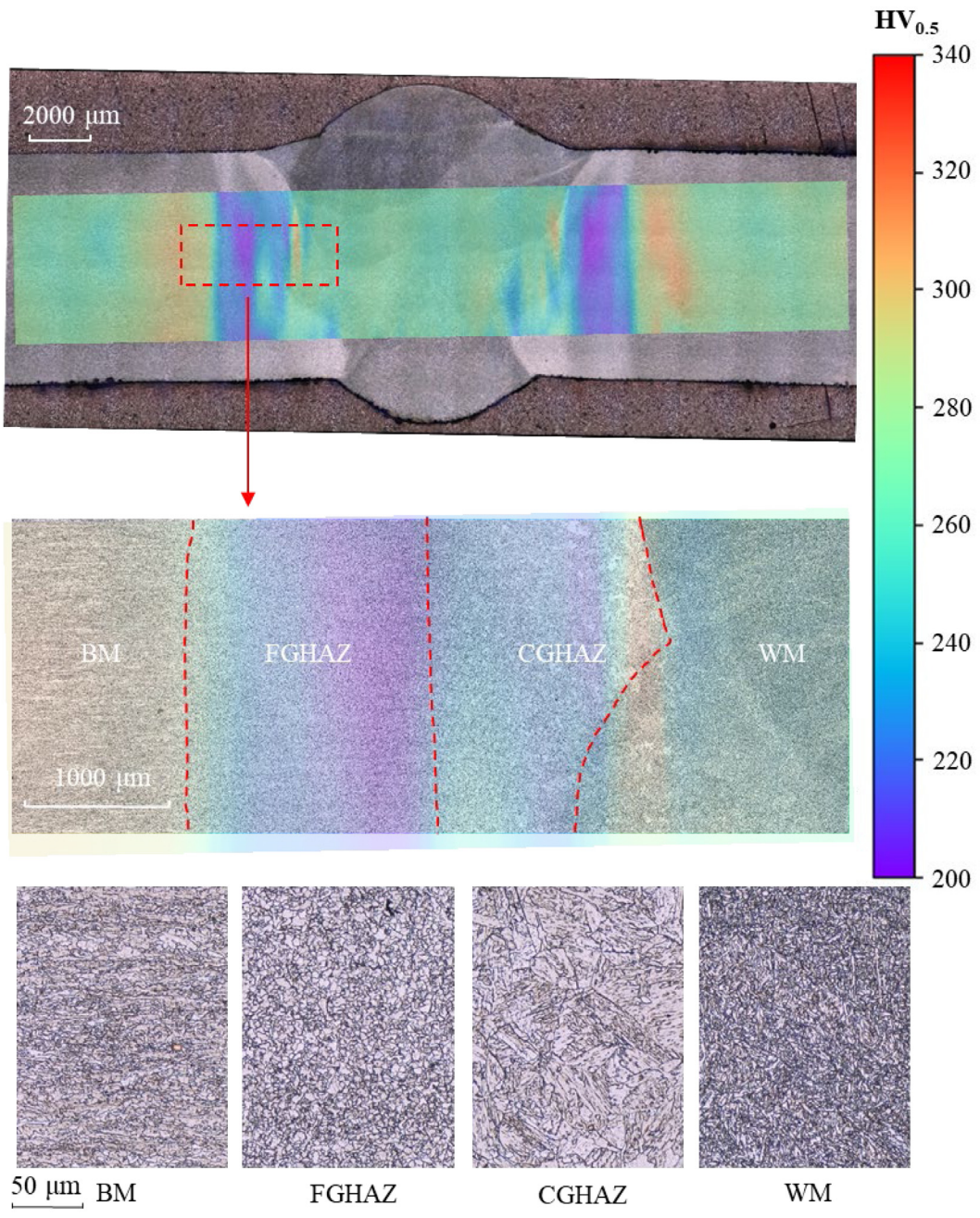
HV0.5
340
320
300
280
260
240
220
200
2000 µm
BM
FGHAZ
CGHAZ
WM
1000 µm
50 µm
BM
FGHAZ
CGHAZ
WM

h) S700t8N2.

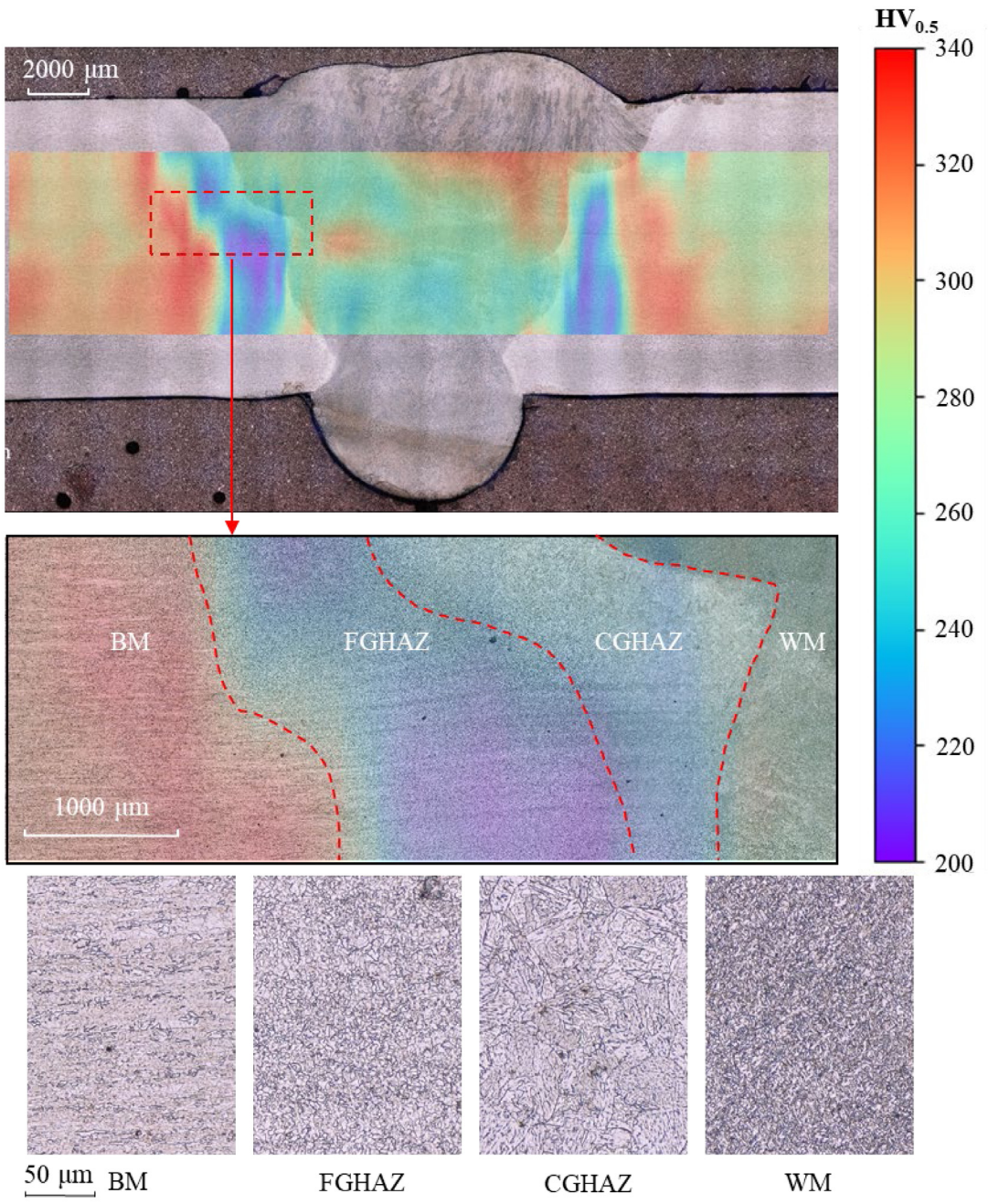
HV0.5
340
320
300
280
260
240
220
200
2000 µm
BM
FGHAZ
CGHAZ
WM
1000 µm
50 µm
BM
FGHAZ
CGHAZ
WM

i) S700t10N2.

References

[1] M. Amraei, A. Ahola, S. Afkhami, T. Björk, A. Heidarpour, X.L. Zhao, Effects of heat input on the mechanical properties of butt-welded high and ultra-high strength steels, Eng. Struct. 198 (2019) http://dx.doi.org/10.1016/j.engstruct.2019.109460.

[2] H.C. Ho, K.F. Chung, M.X. Huang, D.A. Nethercot, X. Liu, H. Jin, G.D. Wang, Z.H. Tian, Mechanical properties of high strength S690 steel welded sections through tensile tests on heat-treated coupons, J. Construct. Steel Res. 166 (2020) 105922, http://dx.doi.org/10.1016/j.jcsr.2019.105922.

[3] X. Liu, K.F. Chung, H.C. Ho, M. Xiao, Z.X. Hou, D.A. Nethercot, Mechanical behavior of high strength S690-QT steel welded sections with various heat input energy, Eng. Struct. 175 (2018) 245–256, http://dx.doi.org/10.1016/j.engstruct.2018.08.026.

[4] W. Cai, Y. Wang, G. Li, R. Stroetmann, Comparative study on strength of TMCP and QT high-strength steel butt-welded joints, J. Construct. Steel Res. 197 (2022) 107447, http://dx.doi.org/10.1016/j.jcsr.2022.107447.

[5] R. Yan, H. Xin, F. Yang, H. El Bamby, M. Veljkovic, K. Mela, A method for determining the constitutive model of the heat-affected zone using digital image correlation, Constr. Build. Mater. (2022) http://dx.doi.org/10.1016/j.conbuildmat.2022.127981.

[6] V.P. Nguyen, Effect of heat input on the mechanical properties of welded joints, 2018, https://urn.fi/URN:NBN:fi:amk-2018091915234.

[7] H.G. Pisarski, R.E. Dolby, The significance of softened HAZs in high strength structural steels, Weld. Res. Abroad 50 (2003) 22–30.

[8] F. Hochhauser, W. Ernst, R. Rauch, R. Vallant, Influence of the soft zone on the strength of welded modern HSLA steels, Weld. World 56 (2012) http://dx.doi.org/10.1007/BF03321352.

[9] M. Khurshid, Z. Barsoum, I. Barsoum, Load carrying capacities of butt welded joints in high strength steels, J. Eng. Mater. Technol. Trans. ASME 137 (2015) 1–9, http://dx.doi.org/10.1115/1.4030687.

[10] R. Yan, H. El Bamby, M. Veljkovic, H. Xin, F. Yang, A method for identifying the boundary of regions in welded coupon specimens using digital image correlation, Mater. Des. 210 (2021) 110073, http://dx.doi.org/10.1016/j.matdes.2021.110073.

[11] EN 1993-1-8:2005 - Design of steel structures - Part 1-8: Design of joints, 2005.

[12] PrEN 1993-1-8:2021 - Design of steel structures - Part 1-8: Design of joints (draft of EN1993-1-8: 2021), 2022.

[13] H.W. Swift, Plastic instability under plane stress, J. Mech. Phys. Solids 1 (1952) 1–18, http://dx.doi.org/10.1016/0022-5096(52)90002-1.

[14] R.M. Molak, K. Paradowski, T. Brynk, L. Ciupinski, Z. Pakiela, K.J. Kurzydlowski, Measurement of mechanical properties in a 316L stainless steel welded joint, Int. J. Press. Vessels Pip. 86 (2009) 43–47, http://dx.doi.org/10.1016/j.ijpvp.2008.11.002.

[15] J. Kim, Y.-W. Kim, B.-S. Kang, S.-M. Hwang, Finite element analysis for bursting failure prediction in bulge forming of a seamed tube, Finite Elem. Anal. Des. 40 (2004) 953–966, http://dx.doi.org/10.1016/j.

[16] M. Flansbjer, T. Sjögren, Using digital image correlation techniques and finite element models for strain-field analysis of a welded aluminium structure, Appl. Mech. Mater. 70 (2011) 123–128, http://dx.doi.org/10.4028/www.scientific.net/AMM.70.123.

[17] Y. Peng, C. Wu, J. Gan, J. Dong, Characterization of heterogeneous constitutive relationship of the welded joint based on the stress-hardness relationship using micro-hardness tests, Constr. Build. Mater. 202 (2019) 37–45, http://dx.doi.org/10.1016/j.conbuildmat.2018.12.218.

[18] M. Amraei, S. Afkhami, V. Javaheri, J. Larkiola, T. Skriko, T. Björk, X.L. Zhao, Mechanical properties and microstructural evaluation of the heat-affected zone in ultra-high strength steels, Thin-Walled Struct. 157 (2020) http://dx.doi.org/10.1016/j.tws.2020.107072.

[19] A.P. Reynolds, F. Duvall, Digital image correlation for determination of weld and base metal constitutive behavior, Weld. J. (Miami Fla) 78 (1999) 355–s.

[20] W.D. Lockwood, B. Tomaz, A.P. Reynolds, Mechanical response of friction stir welded AA2024: Experiment and modeling, Mater. Sci. Eng. A 323 (2002) 348–353, http://dx.doi.org/10.1016/S0921-5093(01)01385-5.

[21] W.D. Lockwood, A.P. Reynolds, Simulation of the global response of a friction stir weld using local constitutive behavior, Mater. Sci. Eng. A 339 (2003) 35–42, http://dx.doi.org/10.1016/S0921-5093(02)00116-8.

[22] M.A. Sutton, J.H. Yan, S. Avril, F. Pierron, S.M. Adeeb, Identification of heterogeneous constitutive parameters in a welded specimen: Uniform stress and virtual fields methods for material property estimation, Exp. Mech. 48 (2008) 451–464, http://dx.doi.org/10.1007/s11340-008-9132-6.

[23] R. Bai, Y. Wei, Z. Lei, H. Jiang, W. Tao, C. Yan, X. Li, Local zone-wise elastic–plastic constitutive parameters of laser-welded aluminium alloy 6061 using digital image correlation, Opt. Lasers Eng. 101 (2018) 28–34, http://dx.doi.org/10.1016/j.optlaseng.2017.09.023.

[24] X. Wu, J. Shuai, K. Xu, Z. Lv, Local constitutive behavior of undermatched welded joints in pipeline steel using digital image correlation technology, J. Pressure Vessel Technol. Trans. ASME 142 (2020) 1–6, http://dx.doi.org/10.1115/1.4047271.

[25] Y. Peng, C. Wu, J. Gan, J. Dong, Determination of the local constitutive properties of the welded steel joints using digital image correlation method, Constr. Build. Mater. 171 (2018) 485–492, http://dx.doi.org/10.1016/j.conbuildmat.2018.03.182.

[26] G. Li, F. Xu, G. Sun, Q. Li, Identification of mechanical properties of the weld line by combining 3D digital image correlation with inverse modeling procedure, Int. J. Adv. Manuf. Technol. 74 (2014) 893–905, http://dx.doi.org/10.1007/s00170-014-6034-x.

[27] M.I. Costa, D.M. Rodrigues, C. Leitão, Analysis of AA 6082-T6 welds strength mismatch: stress versus hardness relationships, Int. J. Adv. Manuf. Technol. 79 (2015) 719–727, http://dx.doi.org/10.1007/s00170-015-6866-z.

[28] C. Leitão, I. Galvão, R.M. Leal, D.M. Rodrigues, Determination of local constitutive properties of aluminium friction stir welds using digital image correlation, Mater. Des. 33 (2012) 69–74, http://dx.doi.org/10.1016/j.matdes.2011.07.009.

[29] G. Seon, A. Makeev, J.D. Schaefer, B. Justusson, Measurement of interlaminar tensile strength and elastic properties of composites using open-hole compression testing and digital image correlation, Appl. Sci. (Switzerland) 9 (2019) http://dx.doi.org/10.3390/app9132647.

[30] K. Denys, S. Coppieters, M. Seefeldt, D. Debruyne, Multi-DIC setup for the identification of a 3D anisotropic yield surface of thick high strength steel using a double perforated specimen, Mech. Mater. 100 (2016) 96–108, http://dx.doi.org/10.1016/j.mechmat.2016.06.011.

[31] A. Lattanzi, A. Piccininni, P. Guglielmi, M. Rossi, A fast methodology for the accurate characterization and simulation of laser heat treated blanks, Int. J. Mech. Sci. 192 (2021) 106134, http://dx.doi.org/10.1016/j.ijmecsci.2020.106134.

[32] G. Le Louëdec, F. Pierron, M.A. Sutton, Reynolds, Identification of the local elasto-plastic behavior of FSW welds using the virtual fields method, 2013, pp. 849–859, http://dx.doi.org/10.1007/s11340-012-9679-0.

[33] A. Khalfallah, Experimental and numerical assessment of mechanical properties of welded tubes for hydroforming, Mater. Des. 56 (2014) 782–790, http://dx.doi.org/10.1016/j.matdes.2013.11.051.

[34] M.L. Zhu, F.Z. Xuan, Correlation between microstructure, hardness and strength in HAZ of dissimilar welds of rotor steels, Mater. Sci. Eng. A 527 (2010) 4035–4042, http://dx.doi.org/10.1016/j.msea.2010.03.066.

[35] C. Chen, S.P. Chiew, M.S. Zhao, C.K. Lee, T.C. Fung, Welding effect on tensile strength of grade S690Q steel butt joint, J. Constr. Steel Res. 153 (2019) 153–168, http://dx.doi.org/10.1016/j.jcsr.2018.10.009.

[36] C. Chen, S.P. Chiew, M.S. Zhao, C.K. Lee, T.C. Fung, Influence of cooling rate on tensile behaviour of S690Q high strength steel butt joint, J. Constr. Steel Res. 173 (2020) 106258, http://dx.doi.org/10.1016/j.jcsr.2020.106258.

[37] EN ISO 3834-2:2006 Quality requirements for fusion welding of metallic materials - Part 2: Comprehensive quality requirements, 2006.

[38] Metallic materials - Tensile testing - Part 1: Method of test at room temperature (ISO 6892-1:2019), 2019, p. 1.

[39] NEN-EN-ISO 6507-1 Metallic materials - Vickers hardness test - Part 1: Test method, 2018, p. 1.

[40] NEN-EN-ISO 6507-4 Metallic materials - Vickers hardness test - Part 4: Tables of hardness values, 2018, p. 4.

[41] B. Adegeest, Material factors for high strength rectangular hollow section X joints, 2020.

[42] ABAQUS, Abaqus Analysis User's Manual, 2019 Version, 2019.